

COLOR–LUMINOSITY RELATIONS FOR THE RESOLVED HOT STELLAR POPULATIONS IN THE CENTERS OF M 31 AND M 32[†]

THOMAS M. BROWN

Laboratory for Astronomy & Solar Physics, Code 681, NASA/GSFC
Greenbelt, MD 20771
tbrown@band1.gsfc.nasa.gov

HENRY C. FERGUSON

Space Telescope Science Institute
3700 San Martin Drive, Baltimore, MD 21218
ferguson@stsci.edu

S. A. STANFORD

Institute of Geophysics and Planetary Physics, Lawrence Livermore National Laboratory
Livermore, CA 94550
adam@igpp.llnl.gov

AND

JEAN-MICHEL DEHARVENG

Laboratoire d'Astronomie Spatiale du CNRS, Traverse du Siphon, BP 8
F-13376 Marseille Cedex 12, France
jmd@astrsp-mrs.fr

To be published in The Astrophysical Journal

ABSTRACT

We present *Faint Object Camera (FOC)* ultraviolet images of the central $14 \times 14''$ of Messier 31 and Messier 32. The hot stellar population detected in the composite UV spectra of these nearby galaxies is partially resolved into individual stars, and their individual colors and apparent magnitudes are measured. We detect 433 stars in M 31 and 138 stars in M 32, down to detection limits of $m_{F275W} = 25.5$ mag and $m_{F175W} = 24.5$ mag. We investigate the luminosity functions of the sources, their spatial distribution, their color-magnitude diagrams, and their total integrated far-UV flux. Comparison to *IUE* and *HUT* spectro-photometry and *WFPC2* stellar photometry indicates consistency at the 0.3 mag level, with possible systematic offsets in the *FOC* photometry at a level less than this. Further calibrations or observations with the *Space Telescope Imaging Spectrograph (STIS)* will be necessary to resolve the discrepancies. Our interpretation rests on the assumption that the published *FOC* on-orbit calibration is correct.

Although M 32 has a weaker UV upturn than M 31, the luminosity functions and color-magnitude diagrams of M 31 and M 32 are surprisingly similar, and are *inconsistent* with a majority contribution from any of the following: PAGB stars more massive than $0.56 M_{\odot}$ (with or without associated planetary nebulae), main sequence stars, or blue stragglers.

Both the luminosity functions and color-magnitude diagrams are *consistent* with a dominant population of stars that have evolved from the extreme horizontal branch (EHB) along tracks with masses between 0.47 and $0.53 M_{\odot}$. These stars are well below the detection limits of our images while on the zero-age EHB, but become detectable while in the more luminous (but shorter) AGB-Manqué and post-early asymptotic giant branch (PEAGB) phases. The *FOC* observations require that only a very small fraction of the main sequence population (2% in M 31 and 0.5% in M 32) in these two galaxies evolve through the EHB and post-EHB phases, with the remainder evolving through bright PAGB evolution that is so rapid that few if any stars are expected in the small field of view covered by the *FOC*. A model with a flat EHB star mass distribution reproduces the *HUT* and *IUE* spectra of these two galaxies reasonably well, although there is some indication that an additional population of very hot ($T_{\text{eff}} > 25000$ K) EHB stars may be needed to reproduce the *HUT* spectrum of M 31 near the Lyman limit, and to bring integrated far-UV fluxes of M 31 and M 32 into agreement with *IUE*.

In addition to the post-EHB population detected in the *FOC*, we find a minority population ($\sim 10\%$) of brighter stars that populate a region of the CMD that cannot be explained by canonical post-HB evolutionary tracks. The nature of these stars remains open to interpretation.

The spatial distributions of the resolved UV-bright stars in both galaxies are more centrally concentrated than the underlying diffuse emission, implying that stellar populations of different age and/or metallicity might be responsible for each component.

Subject headings: galaxies: evolution — galaxies: abundances — galaxies: stellar content — ultraviolet: galaxies — ultraviolet: stars

[†] Based on observations with the NASA/ESA Hubble Space Telescope obtained at the Space Telescope Science Institute, which is operated by the Association of Universities for Research in Astronomy, Incorporated, under NASA contract NAS 5-26555.

1. INTRODUCTION

The spectra of elliptical galaxies and spiral galaxy bulges exhibit a strong upturn shortward of 2700 Å, dubbed the “UV upturn.” At the time of its discovery, the existence of a hot stellar component went against the traditional picture of early-type galaxies. The canonical view of ellipticals held that these galaxies contained a cool, passively evolving population of old stars. The pioneering UV observations of ellipticals – with the *Orbiting Astronomical Observatory (OAO)* (Code & Welch 1979) and the *International Ultraviolet Explorer (IUE)* (Bertola, Cappacioli, & Oke 1982) – could only sample the Rayleigh-Jeans tail of the hot UV flux, with poor signal-to-noise and resolution. Early explanations for the source of the UV upturn covered a wide range of candidates, including massive young stars, hot horizontal branch stars, planetary nebula nuclei, and several binary scenarios (see Greggio & Renzini 1990 for a complete review). The presence of young stars would imply ongoing star formation in early-type galaxies, while the evolved candidates suggested that old stellar populations could be efficient UV emitters.

Characterized by the $m_{1550} - V$ color, the UV upturn shows surprisingly strong variation (ranging from 2.05–4.50 mag) in nearby quiescent early-type galaxies (Bertola et al. 1982; Burstein et al. 1988), even though the spectra of ellipticals at longer wavelengths are qualitatively very similar. A large sample of UV measurements demonstrated that the UV upturn is positively correlated with the strength of Mg₂ line absorption in the V band, in the sense that the $m_{1550} - V$ color is bluer at higher line strengths, opposite to the behavior of optical color indices (Burstein et al. 1988). Opposing theories have been devised to explain this correlation. For example, Lee (1994) and Park & Lee (1997) suggest that the UV flux originates in the low metallicity tail of an evolved stellar population with a wide metallicity distribution. Their reasoning is that the more massive ellipticals formed earlier, and that it is actually the *mean* metallicity that is higher (and driving the optical indices) in the older and bluer galaxies. In contrast, several groups (Brocato et al. 1990; Bressan, Chiosi, & Fagotto 1994; Greggio & Renzini 1990; Horch, Demarque, & Pinsonneault 1992; Brown et al. 1997; Yi, Demarque, & Oemler 1997) argue that metal-rich horizontal branch stars and their progeny are responsible for the UV flux. Under the metal-rich hypothesis, the canonical trend in horizontal branch morphology (i.e., redder HBs with higher metallicity) is reversed at high metallicity, due to increased helium abundance and possibly a higher mass loss rate on the red giant branch, resulting in the production of hot UV-efficient stars on the extreme horizontal branch (EHB). These hypotheses lead to different ages for the stellar populations in these galaxies. Ages exceeding those of Galactic globular clusters are required under the low-metallicity Park & Lee (1997) hypothesis, while ages as low as 8 Gyr are allowed in the Bressan et al. (1994) model. In these two scenarios, the EHB stars are drawn from either tail of the metallicity distribution. However, it is also possible, indeed perhaps more likely, that the EHB stars arise from progenitors near the peak of the metallicity distribution (cf. Dorman, O’Connell, & Rood 1995), but represent a relatively rare occurrence. The correlation of $m_{1550} - V$ with the global metallicity of the galaxy might indicate that this rare path of stellar evolution becomes less so at high metallicity and helium abundance.

The *Hopkins Ultraviolet Telescope (HUT)*, designed for medium resolution (≈ 3 Å) spectroscopic observations of faint

extended UV sources down to the Lyman limit at 912 Å, offered a new perspective on these populations. With observations of two galaxies on the Astro-1 mission (M 31 and NGC 1399), Ferguson et al. (1991) demonstrated that young, massive stars cannot be a significant contributor to the UV upturn. There is a lack of strong C IV absorption expected from such stars, and the continuum flux decreases from 1050 Å down to the Lyman limit. Such a decrease implies that the UV flux is dominated by stars with temperatures ≤ 25000 K and is incompatible with emission by a population of young stars having a normal initial mass function. Ferguson et al. (1991) also suggested that a bimodal distribution on the horizontal branch was needed to reproduce the shape of spectra from the near-UV to the far-UV, otherwise the spectra would be flatter than observed. Six more galaxies were observed on the Astro-2 mission (M 49, M 60, M 87, M 89, NGC 3115, and NGC 3379), and with these data Brown et al. (1997) demonstrated that a two-component population of high-metallicity post-HB stars could reproduce the UV light seen in nearby ellipticals. In this model, most ($> 80\%$) of the UV-producing stars were undergoing post-asymptotic-giant-branch (PAGB) evolution, and the remainder were evolving along AGB-Manqué paths from the extreme horizontal branch. Although in the minority, these AGB-Manqué stars can produce the majority of the flux, because their lifetimes are orders of magnitude longer than those of the PAGB stars.

Because even the brightest of these galaxies are faint and extended in the UV, studies of the UV upturn have focused mostly on the composite spectral energy distributions of ellipticals. However, the UV imaging capabilities of *HST* have now opened the possibility of studying the resolved UV population, at least in the nearest galaxies. Attempts to do this prior to the *HST* refurbishment were undertaken by King et al. (1992), for M 31, and by Bertola et al. (1995), for M 31 and M 32.

King et al. (1992) obtained a pre-COSTAR *Faint Object Camera (FOC)* observation of a $44 \times 44''$ field in the center of M 31, using the F175W filter and the F/48 relay. They found more than 100 sources that they identified as PAGB stars. Intermediate-mass ($M > 0.6 M_{\odot}$) PAGB stars are short-lived, and given a population size constrained by the fuel consumption theorem, the large number of detected stars implied that these were low-mass PAGB stars. King et al. (1992) estimated that these stars accounted for approximately 20% of the UV light, with the rest unresolved, presumably coming from EHB stars and their AGB-Manqué descendants, which could account for this unresolved light without violating fuel consumption constraints.

Bertola et al. (1995) used the *FOC* to image M 31, M 32, and NGC 205 with the combination of the F150W and F130LP filters on the F/48 relay. Although the optical luminosity enclosed by the *FOC* field was higher in M 32 than in M 31, they found far fewer UV sources in the M 32 field. Because M 32 has a weaker UV upturn and lower metallicity, the UV light was expected to originate in PAGB stars of higher mass (and shorter lifetimes) than those in M 31; so, the relative numbers of detected sources were in line with these expectations. However, the luminosity functions in M 31 and M 32 appeared similar, in contrast to expectations when comparing a population of less massive PAGB stars to a population of more massive ones. Such a puzzle may be partly explained if the PAGB stars are enshrouded in dust during the early part of their evolution away from the AGB.

Both previous *FOC* studies faced daunting challenges in untangling the uncertainties in the *FOC* sensitivity calibration and the red leak of the filters. King et al. (1992) adopted the best in-flight calibration at the time, and used ground calibrations of the filter and photocathode response to assess the effects of red leak. They also determined that the pre-COSTAR PSF required a huge aperture correction of 2.6 mag. Bertola et al. (1995) derived an independent calibration based upon *IUE* observations of NGC 205, M 31, and M 32. In the Bertola et al. calibration, the nominal *FOC* F150W+F130LP efficiency curve required multiplication by factors of 0.21–0.92 (varying with wavelength) in order to produce agreement between the *FOC* and *IUE*. Checking their revised calibration against common stars in the King et al. (1992) F175W images, Bertola et al. determined that the F175W efficiency curve also required revision, such that the peak in the efficiency curve was at 28% of its nominal value, but with increased red leak from longer wavelengths. We demonstrate in §3.3.1 that the pre-COSTAR *FOC* data calibration was seriously in error.

We have used the refurbished, recalibrated *FOC* to follow up these earlier studies with deeper UV images of the M 31 and M 32 cores, in order to further characterize the evolved stellar populations in these galaxies. Our observations use the F175W and F275W filters to determine color-luminosity relationships in these galaxies, and to compare them to the predictions of stellar evolutionary theories.

2. OBSERVATIONS

In February of 1994 and 1995, we obtained *Faint Object Camera (FOC)* ultraviolet images of the giant spiral galaxy Messier 31 (M 31, NGC 224) and its compact elliptical companion, Messier 32 (M 32, NGC 221). In comparison to the other galaxies with measured UV upturn strengths, M 31 and M 32 show relatively weak upturns, with respective $m_{1550} - V$ colors of 3.51 and 4.50 mag (Burstein et al. 1988). Our images are shown in Figures 1 and 2 (Plates XX and YY), as combined with archival *Wide Field Planetary Camera 2 (WFPC2)* data in the optical (F555W) filter. Although the images each include the background from the bright galaxy core, we can clearly resolve many of the hot post-horizontal branch (post-HB) stars that are responsible for the UV light. Our observations were with the *FOC* F/96 relay, using the 512×1024 zoomed format ($512z \times 1024$); this format provided the full $14 \times 14''$ field of view at the expense of the full dynamic range available in the *FOC*. Thus, after processing via the standard pipeline, the frames required dewrapping of brightly illuminated pixels. Once dewrapped, the frames from a given band were aligned and coadded. The observations are summarized in Table 1.

Because the standard pipeline processing applies a dezooming of the pixels (from 512×1024 to 1024×1024) and a geometric correction, the signal in neighboring pixels is correlated, and so the noise characteristics of these images significantly deviate from the Poisson distribution. Well-defined source detection required modelling of the noise characteristics in the images, especially given the presence of a nonuniform background from the underlying galaxies. To simulate the *FOC* noise characteristics, we applied the same dezooming and geometric correction to a set of uniform frames that had Poisson noise; this set of test frames covered the range of signal appropriate to our galaxy images. We then fit a second-order polynomial to the pixel-to-pixel variance in each simulation; the fit is shown in Figure 3. Poisson statistics significantly overestimate the noise

in this format up to a signal of approximately 500 counts per pixel, and underestimate the noise beyond this level.

We fit the full-width half maximum (FWHM) of the point spread function (PSF) in each image using a selection of isolated stars. The fits were performed with the IRAF routine FITPSF, and the results are listed in Table 1. It appears that the focus was slightly better in the M 32 images, perhaps due to “breathing” in the telescope structure. The sharpness of the PSF is known to improve at longer wavelengths, so it is not surprising that the F175W images show wider PSFs as compared to the F275W images. We note that the PSF does not appear to vary significantly with position in the *FOC* field. Our fits to the PSF were used to determine source detection criteria, to simulate completeness, and to simulate spurious source detections, all of which are discussed below. None of the sources appear significantly resolved (e.g., as planetary nebulae), although two sources near the top of the M 31 field appear somewhat elongated in both the F175W and F275W images. These two stars have been flagged in our catalog (Table 2), and are discussed further in §3.2. One does not expect to resolve planetary nebulae (PNe) at a distance of 770 kpc. PNe studies (e.g., Schneider & Buckley 1996) show that very few PNe have diameters as large as 0.8 pc, with most smaller than 0.2 pc. At the M 31 distance, a PN with a diameter of 0.2 pc would span four *FOC* pixels.

The in-flight calibration of the *FOC* F175W and F275W filters was done using observations of HZ4 in the 256×256 format, in conjunction with neutral density filters due to count rate limitations (Jedrzejewski 1996). Thus, our exact combination of format and filters has not been calibrated directly, and this may contribute to some of the systematic uncertainties discussed in §3.3.

While the primary purpose of our observations was to study the stellar population, at the same time these new *FOC* images provide the most detailed view of the morphology of the double nucleus of M 31. *Planetary Camera (PC)* observations by Lauer et al. (1993) provided the first clear optical view of the double nucleus, and deconvolved *FOC* UV observations (King, Stanford, & Crane 1995) indicated that the twin peaks are not due to a dust lane in the center of the galaxy. Our own images of M 31 (Plate XX) clearly show the nuclei as separate entities, also without any evidence of a dust lane. The UV-bright nucleus manifests itself as a sharp peak offset from the optically-bright nucleus. The peak is clearly not a point source, but appears to be a tight cluster of UV bright stars. The color of the UV-bright nucleus is $m_{F175W} - m_{F275W} = -0.34$ mag within $0.2''$, consistent with stars of effective temperature 11500 K. For a discussion of the M 31 nuclei and their respective colors, see King et al. (1995) and references therein.

We note that the small field of view does not include any previously published planetary nebulae or globular clusters in the inner regions of M 31 and M 32, according to a search through the SIMBAD database. Observations of these objects are difficult so close to the core of a galaxy.

3. DATA REDUCTION

3.1. Source Detection

Source detection and photometry in the *FOC* images are complicated by the strongly varying background. Most existing photometry packages, even sophisticated ones, require the user to input a uniform counts threshold above which a signal is considered a detection. Setting this threshold at a high level,

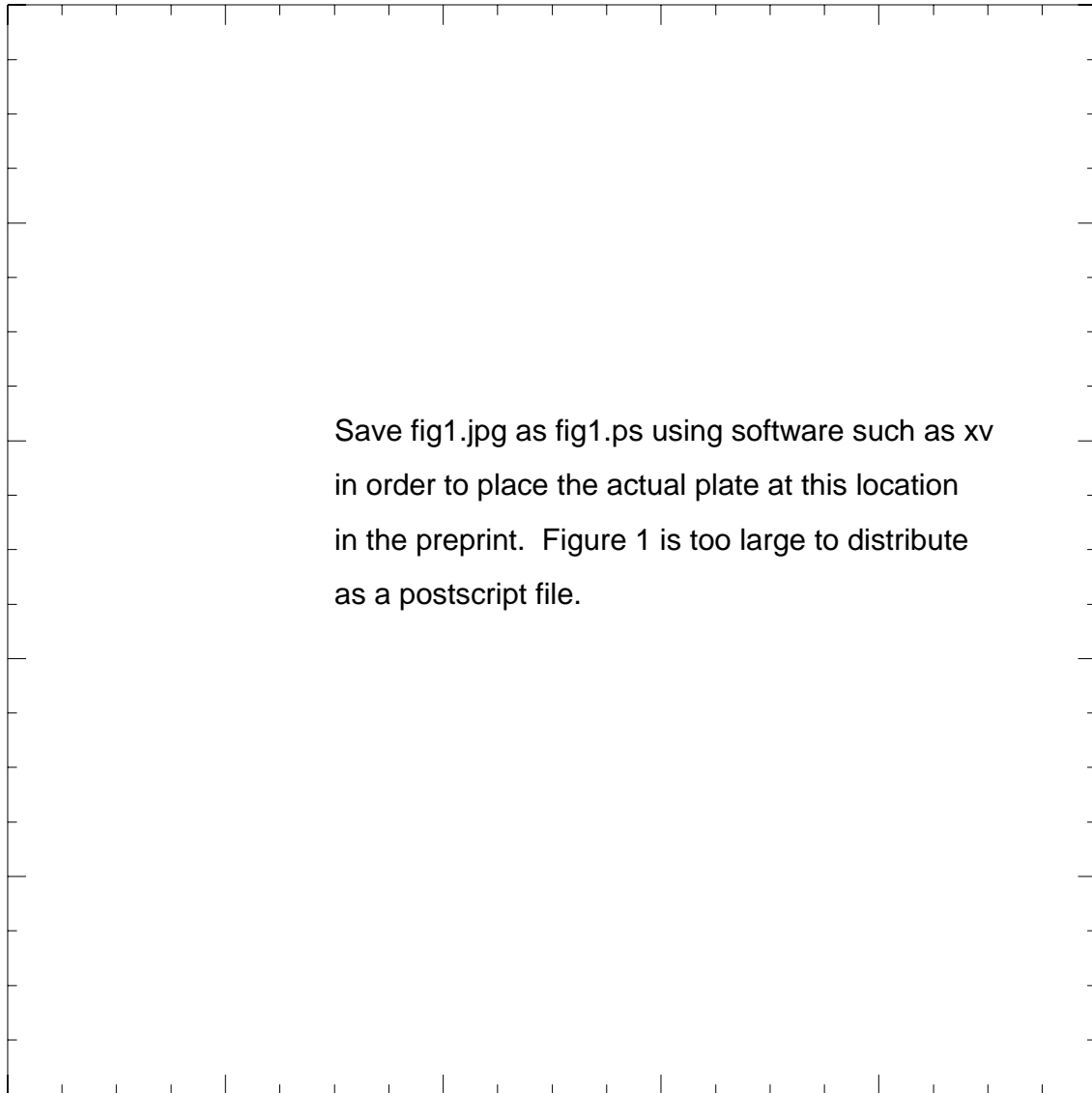


FIG. 1.— This 3-color image of the M 31 center was created by assigning the *FOC* F175W image to the blue, the *FOC* F275W image to the green, and an archival *WFPC2* F555W image (ID# 5464) to the red. The double nucleus is clearly distinguished, with one nucleus brighter in the visible and the other brighter in the UV. The two nuclei are clearly not the result of a dust lane. The hot post-HB stars densely populate the field. We note that the F555W image is saturated in the core.

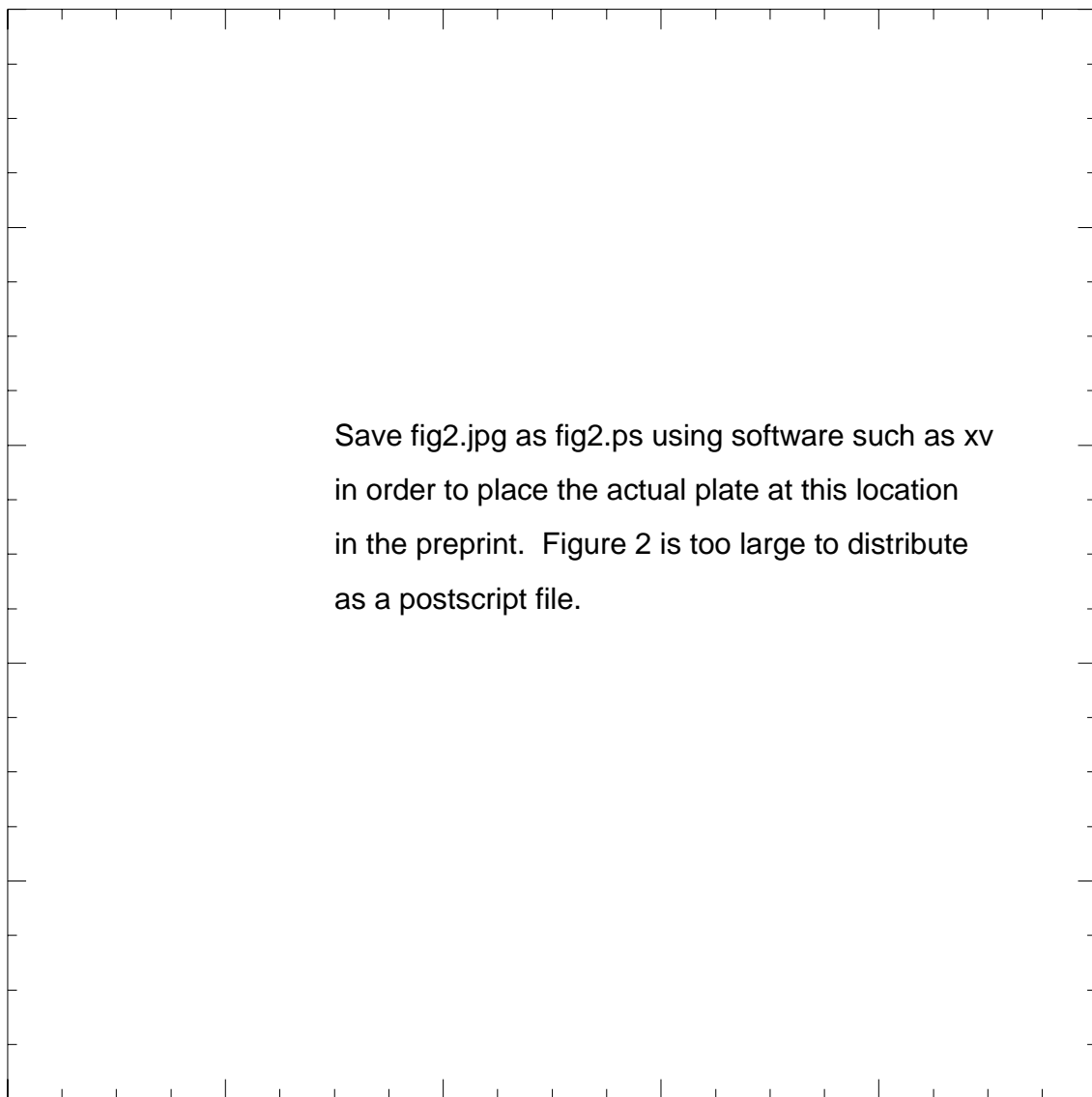


FIG. 2.— The center of M 32, using the same filters as Figure 1 (the F555W archival image again has ID# 5464). In comparison to M 31, the center of M 32 is much smoother and shows far fewer stars. As in the previous figure, the F555W image is saturated in the core.

appropriate to the noise characteristics in the brighter regions of an image, will cause the algorithm to miss fainter sources that should be detectable in the low-background regions of the image. Setting the threshold at a low level, appropriate to the noise in the fainter regions of an image, will cause the algorithm to find many spurious sources in the bright-background regions.

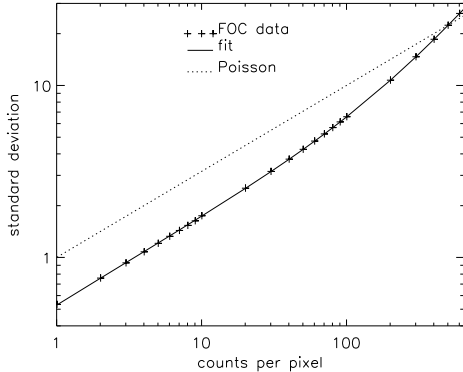


FIG. 3— The noise characteristics of the *FOC* data (crosses) in the F/96 $512z \times 1024$ format deviate significantly from the Poisson distribution (dotted). Our polynomial fit to the *FOC* standard deviation vs. counts (solid) is used to set a spatially constant threshold for source detection in the nonuniform galaxy images (see text).

To work around this difficulty, we produced a galaxy-free, constant-noise image for each band in both galaxies, and used these “detection” images for source detection. The detection images were created by taking the original images, applying a median filter (35×35 pixels), and subtracting the median image from the original. The result was a “galaxy-free” image, but not one with constant noise characteristics. Next, we used our polynomial fit for the variance (Figure 3) to convert the median image into a “noise” image, and divided the galaxy-free image by this noise image. The result was a galaxy-free image where the standard deviation in the background was unity across the entire image. We then applied the IRAF task DAOFIND, provided under the DAO Crowded-Field Photometry Package (DAOPHOTX), setting our detection limit at 4σ . The package looks for local density maxima that meet user-supplied criteria for FWHM, roundness, and sharpness. We left the criteria for roundness and sharpness at the default settings, but after some experimentation, we set the FWHM to 5 pixels for each band. Although the PSF seems to vary somewhat from image to image (see §2 and Table 1), we wanted to be able to detect any nebulae which might not have the narrow PSF of a star. While this procedure is effective at pushing the source detections to the noise limits of the observations, it has the consequence that the limiting magnitude is a function of position. For most of the subsequent discussion, we limit ourselves to the brighter sources and to a region of each galaxy more than $1.5''$ from the nucleus.

DAOFIND produced source lists for each band. Due to the geometric correction, the edges of the *FOC* detector do not coincide with the edges of the image (see Figures 1 & 2). This causes problems with the source detection in the images at the detector boundaries, necessitating the rejection of sources along the edges of the detector (see Figures 4 and 5). We combined the source lists for each band into a master source list for each

galaxy, but retained the information about the band(s) in which each source was detected. Thus, a star that was too faint to be a 4σ detection in the F175W filter but bright in the F275W filter could still produce F175W photometry, and vice versa. These matters complicate the characterization of our completeness vs. magnitude, as we discuss in §3.4. Sources detected in both bands were matched by taking the position in one band and finding the closest detection in the other band within 3 pixels.

3.2. Photometry

We used the STMAG system for our analysis of the *FOC* data. In this system, the image header parameter PHOTFLAM defines the inverse sensitivity. The quantities of interest are:

$$m = -2.5 \times \log_{10} f_{\lambda} - 21.10$$

$$f_{\lambda} = \text{counts} \times \text{PHOTFLAM} / \text{EXPTIME}$$

$$m = -2.5 \times \log_{10}(\text{counts} / \text{EXPTIME}) + m_o$$

where EXPTIME is the exposure time, m_o is the magnitude that produces 1 count per second in the observing mode, and -21.10 is the magnitude corresponding to a flat flux (f_{λ}) of $1 \text{ erg s}^{-1} \text{ cm}^2 \text{ \AA}^{-1}$ in the bandpass. The values of PHOTFLAM, EXPTIME, and m_o for our data are given in Table 1.

For our aperture photometry, we used the IRAF task PHOT, also provided under the DAOPHOTX package. In each band for each galaxy, we used a circular aperture with a radius of 3 pixels ($0.042''$), centered on the coordinates found during detection. If the source was detected in both bands, the coordinates used for the photometry in a given band matched those determined during detection in that band. If the source was detected in only one band, then those coordinates were used for the photometry in both bands. We did not recenter during the photometry, because a star might be very faint in one band while bright in the other, possibly resulting in an erroneous shift to a nearby local maximum in the faint band photometry. Sky subtraction was performed by taking an annulus with an inner radius of 15 pixels and an outer radius of 20 pixels; the background level was taken to be the centroid of the histogram of pixel intensities within that annulus. By applying varying apertures to isolated stars, we found that an aperture correction of -0.56 mag was needed for the F275W photometry and an aperture correction of -0.61 mag was needed for the F175W photometry.

Our photometric catalogs were edited to reject stars within $1.5''$ of the center in each galaxy (see Figures 4 and 5), because the spurious sources found near the cores would be very bright (see §3.4). Furthermore, because a star could be detected in one band but not the other, if the photometry failed in either band for a star, it was also rejected. Failed photometry occurred if the counts in the 3-pixel aperture were not positive after subtraction of the sky background. Our source catalogs are shown in Tables 2 and 3, truncated at the detection limits of $m_{F175W} = 24.5 \text{ mag}$ and $m_{F275W} = 25.5 \text{ mag}$ (see §3.4). We also plot maps of these catalogs in Figures 6 and 7, to show the distribution of these stars in our fields. Note that in Tables 2 and 3, a “:” in a magnitude denotes a measurement on a star that was not originally detected in that band.

The two brightest stars in our photometric catalog for M 31 have been flagged in Table 2 because of photometric problems (the brightest is marked “a” and the next brightest “b”). For consistency, their values in the table are the result of our standard reduction procedure, but there are two problems that would change these values. First, the stars appear somewhat elongated in both *FOC* bands, and thus the aperture corrections

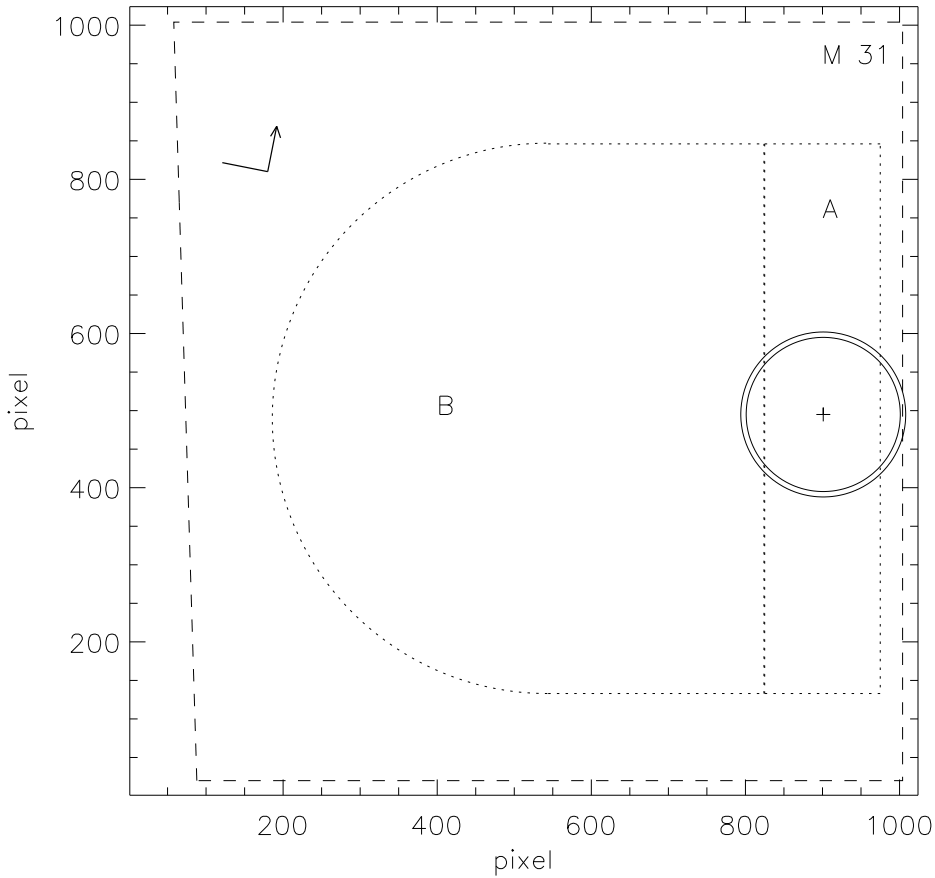


FIG. 4— A schematic of our M 31 analysis clarifies the complicated procedures described in the text. We reject sources near and beyond the edge of the detector (dashed) because the source detection algorithm is confused by the abrupt change at the detector boundary. We also reject sources detected within $1.5''$ (larger circle) of the core (cross). The flux within $1.4''$ (smaller circle) of the core is used to investigate any systematic errors in the *FOC* calibration. Regions “A” (dotted rectangle centered on core) and “B” (dotted semicircle and rectangular region) can be used to approximate the $10 \times 20''$ oval *IUE* aperture, by taking $A+2B$. North and East on the sky are shown by the compass.

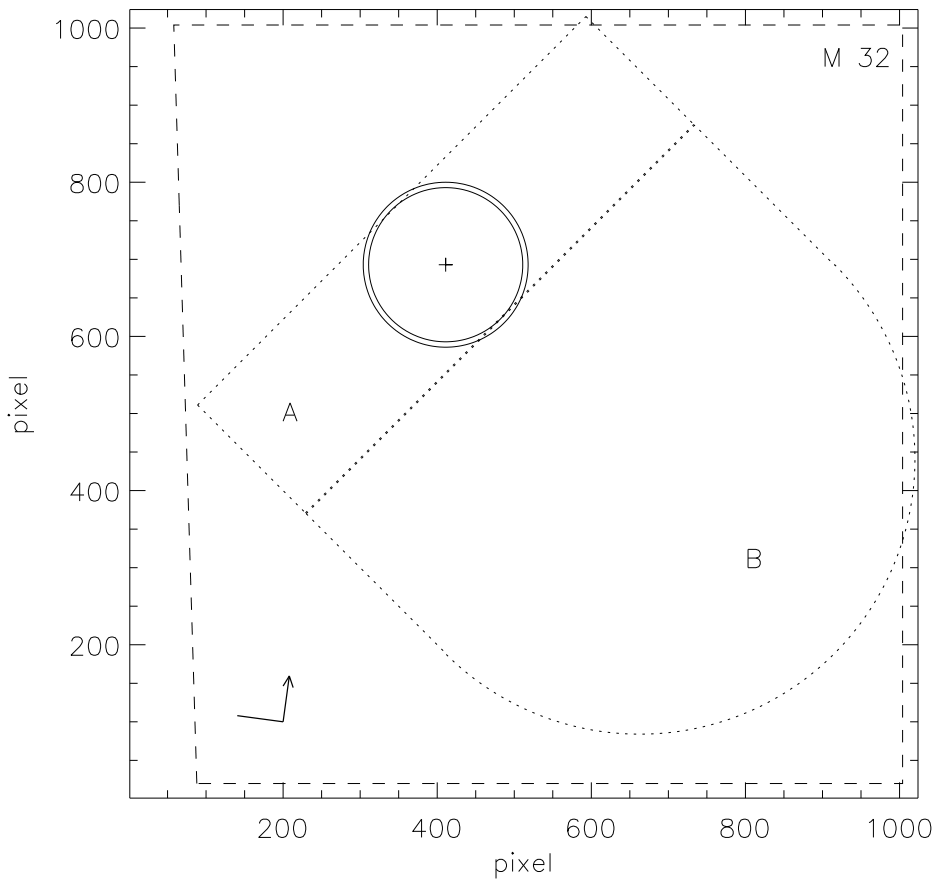


FIG. 5— The same as Figure 4, but for M 32. Because the M 32 core is placed closer to the center of our *FOC* images than was the case with M 31, we define the *IUE* aperture at a different orientation.

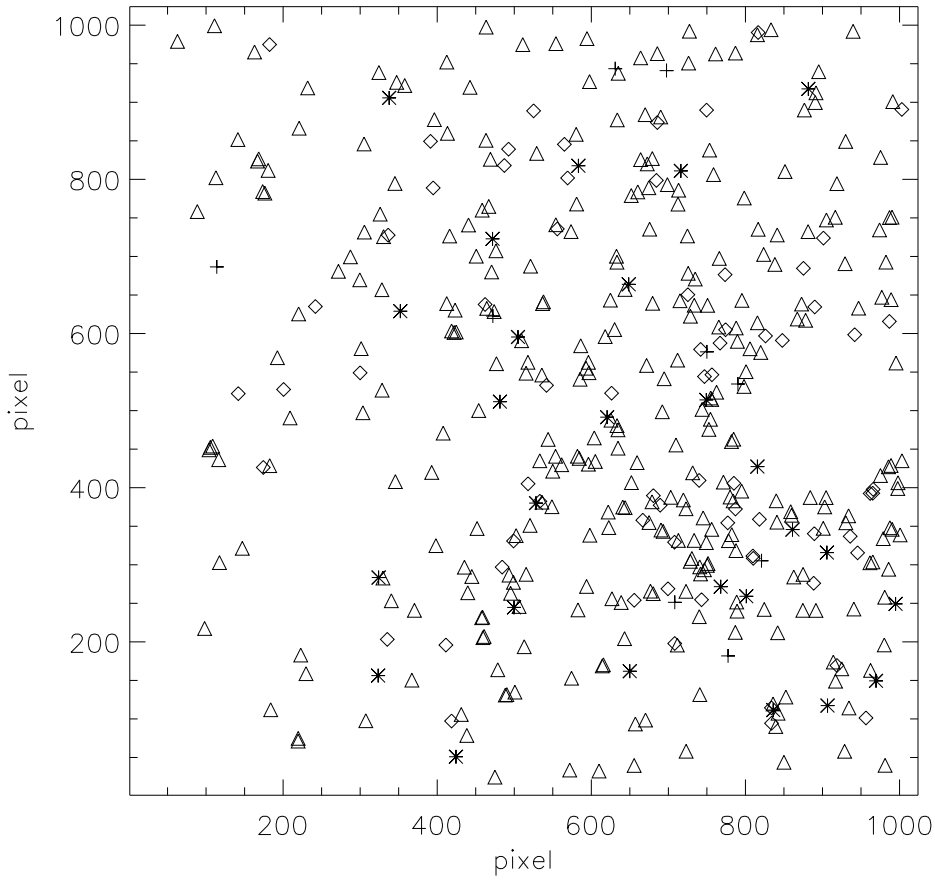


FIG. 6– The photometric catalog of M 31 (Table 2) plotted on the *FOC* field. A cross denotes stars with $20.5 \leq m_{F175W} \leq 21.5$, an asterisk denotes stars with $21.5 \leq m_{F175W} \leq 22.5$, a diamond denotes stars with $22.5 \leq m_{F175W} \leq 23.5$, and a triangle denotes stars with $23.5 \leq m_{F175W} \leq 24.5$.

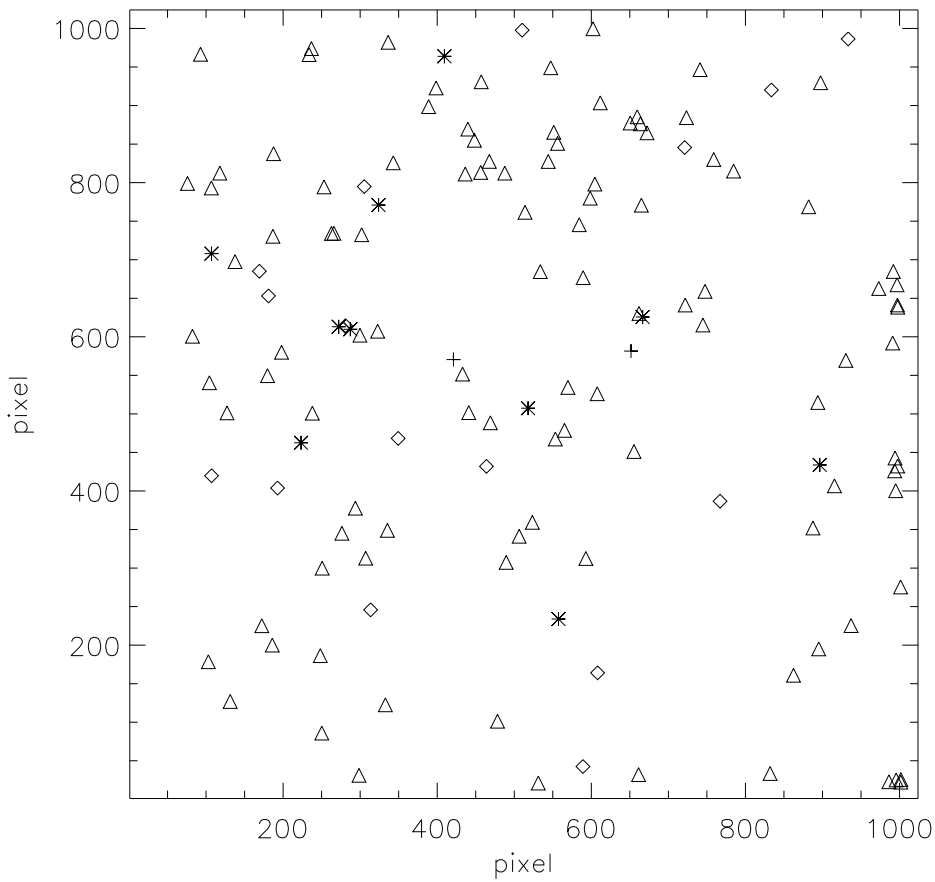


FIG. 7– The photometric catalog of M 32 (Table 3) plotted on the *FOC* field, as in Figure 6.

for each band do not fully correct the 3-pixel flux to the total flux in these stars. Second, the central pixel in each star may have “wrapped” twice instead of once in two out of the three F275W frames (they did not wrap at all in the F175W frames). The additional wraps would require that -0.06 mag be added to the m_{F275W} values for these two brightest stars in the table. The elongation of the stars means that the aperture corrections for star “a” could be -0.97 mag for m_{F175W} and -0.80 mag for m_{F275W} , and the aperture corrections for star “b” could be -0.75 mag for m_{F175W} and -0.68 mag for m_{F275W} , instead of the nominal -0.61 mag and -0.56 mag for m_{F175W} and m_{F275W} . Because it is unlikely that these stars are resolved PNe and because the PSF does not seem to vary with field position (see §2), these stars might be merged images of two or more stars.

We note that the *FOC* cameras suffer from nonlinearity at high count rates (Nota et al. 1996), and that the M 32 F275W image may be affected by this nonlinearity in the galaxy core. For uniform illumination in this format (F/96 $512z \times 1024$), the maximum count rate for linearity is $0.04 \text{ cts s}^{-1} \text{ pix}^{-1}$. Nota et al. defines uniform illumination as varying by “less than 20% over scales of 20 pixels.” The count rate limitation for linearity is much higher in the case of nonuniform illumination from stars, where the central pixel should not have a count rate exceeding $\approx 1 \text{ ct s}^{-1} \text{ pix}^{-1}$. The M 32 core is sharply peaked and varies by more than 20% over scales of 20 pixels, but the core is not nearly as peaked as a stellar PSF. The peak count rate in the core of M 32 is $0.09 \text{ cts s}^{-1} \text{ pix}^{-1}$, and so it is likely that there is some loss of counts in the very center of the M 32 F275W image. However, given its uncertain nature, we do not correct for the nonlinearity. It does not affect our stellar photometry, because we have discarded stars within $1.5''$ of the galaxy center.

3.3. Photometric Uncertainties

Our chosen combination of camera parameters is not frequently used during *FOC* observations. Hence its sensitivity calibration has not been subjected to as many consistency checks as found in other bandpasses. Meurer (1995) estimates that, in general, UV photometry with the *FOC* is accurate to ≈ 0.2 mag. A review of his Instrument Science Report (ISR) and other ISRs available on the Space Telescope Web page (e.g., Jedrzejewski 1996) suggests that systematic errors in calibration of up to ~ 0.2 mag are not implausible.

The absolute calibrations of the F175W and F275W filters were done in a different *FOC* format from our observations, and through neutral density filters (which were calibrated by separate in-flight measurements). Ground-based and in-flight measurements have shown that the *FOC* sensitivity depends on the image format, for reasons that are not completely understood. The format correction for our observations is a multiplicative factor of 1.25, as recommended in Greenfield (1994). The major source of uncertainty in the calibration is this format correction, which should be wavelength independent.

Given these uncertainties, we chose to test how well our *FOC* photometry agrees with other measurements. There are several possible tests: (1) the magnitudes of the brighter point sources can be compared to previous *FOC* results; (2) the magnitudes of the brighter point sources can be compared to photometry of the same sources with *WFPC2*; (3) the total flux of the M 31 and M 32 nuclei can be compared to results from *IUE* and *WFPC2*. We discuss these consistency tests in detail below.

3.3.1. Comparison to Previous *FOC* results

The current calibration of the *FOC* is much more certain than that of the pre-COSTAR *FOC*; the ISRs on the STScI web page describe the various uncertainties in both the pre-COSTAR and refurbished *FOC*. The previous *FOC* observations of M 31 and M 32 utilized the pre-COSTAR F/48 camera, and was subject to two large uncertainties in the calibration. First, the lack of neutral density filters in this mode prevented direct calibrations with *IUE* standard stars (as done for the F/96 camera). Second, the cross-calibrations between F/96 and F/48 were compromised by the early failure of the F/48 detector. On top of these uncertainties unique to the F/48 camera, the photometry in both pre-refurbishment *FOC* cameras required large encircled energy corrections.

With these uncertainties in mind, we compare some of our bright point sources to those found in the M 31 King et al. (1992) analysis. There are 19 stars in the King et al. photometric catalog (King, private communication) that can be found in our own F175W image of M 31. Although our $14 \times 14''$ field contains 31 of the stars found in the $44 \times 44''$ field of King et al., the differences in geometric correction between the old and new cameras prevent us from securely matching all of the King et al. sources to ones in our own field. King et al. (1992) define the correspondence between their magnitudes and the flux at 1750 \AA as:

$$f_{\lambda} = 7.6 \times 10^{-17} \times 10^{-(m-27.60)/2.5}$$

while under the STMAG system, as defined in §3.2, we have

$$f_{\lambda} = 10^{-(m+21.10)/2.5}.$$

The King et al. (1992) fluxes are (on average) a factor of 5.6 higher than ours for sources in common. We suspect that much of this discrepancy is due to the difficulty of working with pre-refurbishment data. Another factor is the format-dependent sensitivity (Greenfield 1994), which was unknown at the time of the King et al. (1992) work. King et al. assumed that the *FOC* sensitivity was 80% of nominal, when in reality the zoomed format was 1.44 times *more* sensitive. Thus, the King et al. (1992) fluxes should be multiplied by $0.8/1.44 = 0.56$, and the factor of five discrepancy with our own measurements falls to a factor of three. In contrast, the Bertola et al. (1995) recalibration makes these stars *brighter* than determined by King et al. (1992). Hence the current *FOC* calibrations imply a substantial revision to the conclusion that the resolved sources in the previous *FOC* images are low-mass PAGB stars.

Although the Bertola et al. (1995) images of M 31 and M 32 include sources in common with our own images, we find that their revisions to the pre-COSTAR F130LP+F150W *FOC* calibration are seriously in error. If the sensitivity of the pre-COSTAR *FOC* was degraded to the level claimed by Bertola et al., 61 stars found in their M 31 image would also be detectable in archival *WFPC2* F160BW images of M 31 (12000 sec exposure) at a S/N ratio of at least 10 (and as high as 30), assuming the stars to be hot ($T_{\text{eff}}=30000 \text{ K}$) PAGB stars. There are no such bright stars in the F160BW image. In contrast, if we use the nominal *FOC* calibration for the stars detected in our own F175W image to predict the count rates in the F160BW, we find that our brightest star would be present at a S/N ratio of 3 in the F160BW, with most having a S/N ratio less than 2. Thus, our photometry is in agreement with the F160BW data, which shows no obvious sources in the field.

Because the previous *FOC* photometry is prone to such large errors, we choose to compare our data with much more reliable *WFPC2* and *IUE* measurements, as discussed in the next two sections.

3.3.2. Comparison to *WFPC2* photometry of point sources

M 31 was observed by *WFPC2* for 3000 sec through the F300W filter and 460 sec through the F336W filter. We reduced the observations following standard procedures, and measured star magnitudes through a $0.14''$ radius aperture, adopting an aperture correction of -0.24 mag (Holtzman et al. 1995). There are 48 bright stars common to all four UV images available (F175W, F275W, F300W, F336W) in the *FOC* and *WFPC2* data. These stars show an average $m_{F175W} - m_{F275W}$ color of -0.26 mag with an rms dispersion of 0.43 mag.

The *FOC* colors correspond to stars with effective temperature 10500 K, on the cool end of the populations we are studying in these *FOC* UV images, but in line with expectations when we are looking at stars that also appear in the redder *WFPC2* filters. A star with an effective temperature of 10500 K would have a $m_{F275W} - m_{F300W}$ color of -0.01 mag, whereas the measured colors average 0.23 mag (rms = 0.34 mag) for these stars, i.e., the *FOC* magnitudes would need to be 0.24 mag brighter to produce *FOC*-to-*WFPC2* colors that agree with the *FOC* colors. At the same effective temperature, the $m_{F300W} - m_{F336W}$ color should be -0.05 mag, and we measure it to be 0.06 (rms 0.47 mag). So, the internal *WFPC2* colors of these 48 stars are more in line with the internal *FOC* colors than the *FOC*-to-*WFPC2* colors. These comparisons would argue that the *FOC* photometric zero-point for our observations is too high. That is, the F275W magnitudes should be brighter than we observe by 0.24 mag. As this is most likely due to the format dependence, such a correction would affect both *FOC* bands. We shall see below that such a correction to the F175W sensitivity would put the F175W fluxes of the two galaxy nuclei rather seriously in disagreement with the *IUE* results.

Taken at face value, the red $m_{F275W} - m_{F300W}$ colors would imply stars of effective temperature 5000 K to 10000 K. This is inconsistent with the blue *FOC* colors for the same sources and with their non-detection in the *WFPC2*. For a star of 5000 K, the count rate in F814W would be 75 times higher than in F300W, and all of these stars would be detected at signal-to-noise ratios of 5–170 in the F814W image. These stars are no brighter than the 5σ level at their positions in the *WFPC2* F814W image.

3.3.3. Comparison to *IUE* and *WFPC2* Photometry of the Nuclei

The integrated fluxes of the central regions of the two galaxies in our *FOC* images can be compared to photometry from *WFPC2* and to fluxes measured by *IUE*. The comparison is complicated by the large corrections that need to be applied to compare the *IUE* and *FOC* fluxes in equivalent aperture sizes.

Unsaturated archival *WFPC2* data for the M 31 and M 32 cores exist in the F160BW, F300W, F336W, F555W, and F814W bands. Unfortunately, in the F160BW filter, M 32 is invisible and M 31 is barely detectable, so we discarded these far-UV *WFPC2* data and used the other *WFPC2* bands. Composite UV+Optical spectra of the cores of M 31 (McQuade, Calzetti, & Kinney 1995) and M 32 (Calzetti, private communication) were fed through the IRAF package SYNPHOT to determine the expected colors of the nucleus as seen in the *FOC*

and *WFPC2* bands available to us (Table 4). These composite spectra were spliced together from aperture-matched *IUE* and ground-based data. The *IUE* aperture sampled a large $10 \times 20''$ area centered on each galaxy nucleus. We extended these spectra beyond 7500 Å, to 12000 Å, by defining a flat continuum that reproduced the *WFPC2* $m_{F555W} - m_{F814W}$ colors in each galaxy. This red extension for each spectrum was only needed to reproduce the red leak contributions properly for the various *FOC* and *WFPC2* filters.

After using SYNPHOT to compute the predicted *FOC* and *WFPC2* count rates for a $10 \times 20''$ aperture centered on the nucleus, we measured the count rate in the archival *WFPC2* data and our own *FOC* data, using an aperture with a diameter of $2.8''$ centered on the galaxy cores (see Figures 4 and 5). We chose an aperture of this smaller size to reduce the systematic errors introduced from our background assumptions. The SYNPHOT predicted count rates were then normalized to agree in the visual (F555W), accounting for the difference in aperture sizes. In Table 4 we show the net count rate in this aperture for each of the images, as well as the gross count rate, dark count rate, and sky count rate. Dark counts were subtracted from the *WFPC2* data in the pipeline processing (hence the zero values in the table); for the *FOC* dark counts, we used the nominal value of 7×10^{-4} cts s^{-1} pix^{-1} from Nota et al. (1996), and this agrees well with the value determined independently from those portions of the detector occulted by the *FOC* “fingers” (see Figures 1 & 2). The sky contributions came from running SYNPHOT with the STScI sky template for high zodiacal and high Earth shine. We chose high sky values because of the small sun-angle during these observations ($\approx 60^\circ$); however, because of the small aperture we are using ($2.8''$ diameter), choosing lower values of sky background would produce negligible changes in our results (Table 4). We note that the *WFPC2* data were cosmic ray rejected using the IRAF package CRREJ, and were also corrected for hot pixels using the IRAF package WARMPIX.

In Table 4, comparison of the predicted *IUE* count rates in each *HST* band vs. the net measured count rates suggests a discrepancy in the F275W flux, in the same sense as that discussed above. That is, it appears that the flux in F275W is about 25% lower than expected, based on the *WFPC2* observations. However, it appears that the F175W flux is reasonably close to expectations based upon *IUE* and *WFPC2* measurements. There is a radial color gradient in each of these galaxies, so we do not expect a completely flat net/predicted ($2.8''/10 \times 20''$) count rate ratio all the way from the UV to the visual; it is evident in Table 4 that these galaxies become redder with increasing radius. However, the F275W count rate is noticeably shifted with respect to the neighboring F175W count rate (in the *FOC*) and the F300W count rate (in the *WFPC2*). The M 31 F275W net/*IUE* count rate ratio requires multiplication by 1.25 in order to bring it into agreement with the ratio in the neighboring bands, and the M 32 F275W net/*IUE* count rate ratio requires multiplication by 1.43. However, the central region of the M 32 F275W image has a count rate that probably falls in the non-linear regime for *FOC* extended sources (see §3.2), and this effect may be decreasing the number of counts measured in the $2.8''$ aperture; the M 31 nucleus should not be suffering from this nonlinearity. Hence, the data in Table 4 might suggest that the nominal F275W values of PHOTFLAM (9.38×10^{-18}) and m_o (21.47 mag) should be respectively multiplied by 1.25 and shifted by -0.24 mag in order to agree with predictions from

IUE.

To summarize, we have compared our *FOC* photometry to photometry from *WFPC2* archival images and to spectrophotometry from *IUE*. We find evidence for systematic discrepancies at the 0.25 mag level. However, applying such a correction would produce stellar colors that are incompatible with *WFPC2* photometry and with plausible stellar evolutionary tracks. As we cannot identify an obvious flaw in the sensitivity calibration (Jedrzejewski 1996) that would lead to a systematic difference between F275W and F175W, we have chosen to adopt the pipeline *FOC* sensitivity calibration with no additional corrections. We must caution that our interpretation rests rather heavily on this calibration. In a sense, we have taken the approach of adopting the nominal calibration to see where it leads, in spite of the disturbing inconsistencies with other observations. Further calibrations of the *FOC* and/or observations of these galaxies with *STIS* will be required to sort out the calibration issues with greater certainty.

3.4. Completeness and Spurious Sources

At the 4σ detection limit, the faint sources in our catalog represent only a small fraction of those actually present in the population. Furthermore, many spurious sources are detected through local maxima in the noise of the background. To properly characterize the completeness of our photometric sample and the contamination from spurious sources, we ran photometry simulations of the *FOC* data.

To characterize the completeness for a given band in one of the galaxies, we created a blank image frame and added 10 stars (one for each magnitude from 21 to 30) at random positions using the PSF sizes listed in Table 1. We then block summed the image along one axis (combining every 2 pixels into one), added Poisson noise, dezoomed the image back to 1024×1024 pixels, and applied the geometric correction for the *FOC*. This process gave the “fake” stars the proper distortion and noise characteristics. We then added this image of fake stars to the true *FOC* image of the galaxy, and performed our source detection and photometry to attempt recovery of these fake stars. The entire simulation was repeated 100 times, and the resulting photometric records allowed us to determine the completeness of our sample as a function of the photometric magnitude. These results are shown in Table 5, along with the standard deviation in the recovered magnitudes. The recovered magnitudes for the fake stars also provided an independent measurement of the aperture correction, and this was in agreement with the correction determined from direct measurement on isolated stars (§3.2).

The spurious source characterization proceeded in a similar manner. Starting with the actual galaxy image, we corrected the flux between the edge of the detector and the image border to match that on the detector, and then applied a 35×35 median filter to remove all of the stars from the image. We then block summed this image along one axis, added Poisson noise, dezoomed, and applied the geometric correction. This last step of applying the geometric correction restores the gap between the detector edge and the image border. Next, we applied our source detection and photometry to this image and recorded the number of stars found at each magnitude from 21 to 30. The simulation was repeated 100 times, and allowed us to determine the average number of spurious sources found at each magnitude (the median filtering of the image meant that any detected source, by definition, would be spurious). We took the average number of spurious sources and divided by the actual number

of sources found in that galaxy image to determine the contamination from spurious sources (Table 5). The contamination at very faint magnitudes exceeds 100% because of slight differences between the simulation “sourceless” images and the real image. For example, a fraction of the area in the real image is taken up by the PSFs of bright stars that are not present in the sourceless images. Also, the median filter will slightly redistribute the flux in the bright stars to the background. Finally, the background in the galaxies is comprised mainly of horizontal branch stars that are below the detection limits, presenting a non-uniform background. Thus, although the simulation sourceless images have very nearly the same background characteristics as the real images, they are not exactly the same, and so the spurious source contamination at faint magnitudes only serves as a guide for the limits to our real photometry.

As evident from Table 5, the completeness and spurious source contamination is very similar for the two galaxies, while a comparison of the different bands shows that the F275W band reaches fainter than the F175W band. Based upon our simulations, we find that our photometry is reliable down to $m_{F175W}=24.5$ mag and $m_{F275W}=25.5$ mag, beyond which the number of detected sources drops rapidly and the contamination from spurious detections increases significantly.

Because the galaxy background varies dramatically over the entire image, and is very large in the cores of the galaxies, our completeness and spurious source contamination is a function of position in each image, and the spurious sources in the very centers of the galaxies are very bright. These bright spurious sources will not be rejected by discarding stars fainter than $m_{F175W}=24.5$ mag and $m_{F275W}=25.5$ mag; the limits only represent the average characteristics of the image. Color magnitude diagrams that include the inner $1.5''$ of each galaxy thus show a well-resolved group of bright sources, separate from the rest of the population. We assume that these sources are spurious (and not an unusual class of stars residing in the galaxy cores), and so we discard sources that lie within $1.5''$ of the center of each galaxy. Our completeness and spurious source contamination, shown in Table 5, reflects the discarding of these sources.

It is important to note that our completeness and spurious source contamination has been defined using detection and photometry in a single band. Without making assumptions about the colors of the stars we are simulating, this is the only way to characterize our photometry. However, our photometric catalog includes more faint stars in each band than expected from the completeness simulations, because a star that is fainter than a 4σ detection in one band might have been detected in the other if it was bright in the other band. For this reason, our luminosity functions (LFs) in each band only include sources that were detected in that band, as discussed in §4.2.

4. ANALYSIS

4.1. Distribution of Diffuse and Stellar Light

If the UV-bright stars are drawn from a population that is different from the diffuse population (either in age or metallicity), differences might be detected in the distribution of diffuse light and stellar light in these galaxies. In Figure 8, we show the distribution of diffuse light as compared to the distribution of light from bright stars.

We define bright stars as those detected at luminosities 1 mag brighter than the detection limits in a given band; e.g., the F275W bright stars are those stars detected in F275W with magnitudes brighter than $m_{F275W} = 24.5$ mag. Fainter stars were

excluded from the analysis to minimize contamination from spurious sources and to ensure that the completeness of the sample did not vary with position in the images. To measure the diffuse light in the *FOC* images, we removed a 4-pixel radius area around each of the bright stars, replacing it with the median value in the area outside of this radius and bounded by a 15×15 pixel square. The diffuse light in each annulus was then measured after subtracting the dark counts and sky background (assuming high zodiacal and high Earth shine, as discussed in §3.3). The distributions of diffuse light and bright stellar light were measured in annuli chosen to keep the number of bright stars in each annulus constant; in this way, the statistical uncertainty in each annulus (due to the small number of bright stars) can be kept approximately constant. There are 25 bright stars in each M 31 annulus, and 7 in each M 32 annulus.

Although the distributions of stars are noisy, it is apparent that the light from UV-bright stars is more tightly concentrated toward the galaxy centers than the diffuse light. The trend has also been seen in previous studies (cf. Bertola et al. 1995). It is well-known that metallicity gradients exist in early-type galaxies, in the sense that the metallicity decreases with distance from the center (cf. González & Gorgas 1995 and references therein). If the UV-bright post-HB stars are more easily produced at higher metallicities, it would make sense that they would fall off more rapidly with radius than the underlying diffuse light. This is because the diffuse light has contributions from the main sequence turnoff and any metal-poor HB population (if present). The luminosity of the main sequence is affected by the metallicity to a much smaller degree, and in the opposite sense (i.e., it becomes brighter at decreasing metallicity); the metal-poor blue HB population would become more prominent as we move outward with decreasing metallicity.

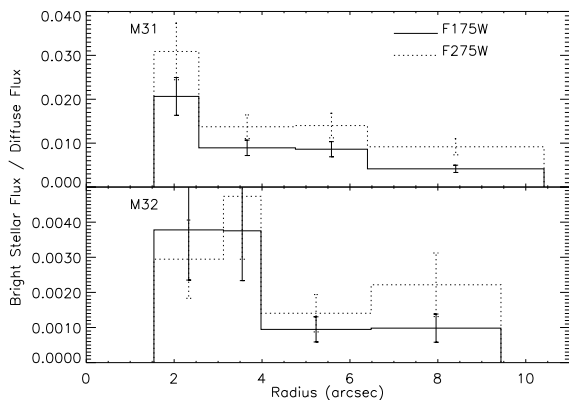


FIG. 8— The ratio of flux in bright stars to the flux in diffuse light shows a rapid decline with radius in the galaxies. UV-bright stars are defined as those 1 mag brighter than the detection limits in each band, and were chosen to ensure that the completeness remained constant with position, and also to reject any spurious sources from our analysis. The sizes of the annuli were chosen to keep the number of stars constant in each annulus, in order to provide fairly uniform statistical uncertainties from bin to bin. Each M 31 annulus contains 25 UV-bright stars, and each M 32 annulus contains 7 UV-bright stars. Error bars reflect statistical uncertainty in both the number of stars and counts, but are dominated by the number of stars.

4.2. Luminosity Functions

The photometric analysis on each galaxy yielded catalogs of stars in M 31 and M 32. However, as noted in §3.1, the catalog in each galaxy is made up of many stars that were detected (at 4σ) in only one band but have photometry in both bands. Without making assumptions regarding the color of the population, we can only characterize our detection limits using simulations in one band (see §3.4), so we create a luminosity function for a given band by drawing upon only those stars in our catalog that were detected in that band. Knowledge of the star from the other band is ignored in this analysis, and so, for example, a bright star in F175W that is fainter than $m_{F275W} = 25.5$ mag will be included in the F175W histogram. In that way, we can compare histograms while using what we know about the completeness and spurious source contamination.

The raw LF for each galaxy in each band is shown in Figure 9. Although we could correct for the completeness and spurious source contamination (Table 5) to plot a “corrected” LF for each band, this is not necessary, because the completeness and spurious source contamination are approximately the same for the different galaxies in each band. The raw LFs can be directly compared without these corrections.

The LFs in a given band look similar when we compare the two galaxies. None of the LFs peak before the sample becomes seriously incomplete and contaminated, but a comparison of the slopes shows no dramatic differences between the stellar populations in each galaxy. From the LFs alone, we could conclude that the UV-to-optical light ratio is weaker in M 32 compared to M 31 simply because there are about half as many UV sources in M 32, and not because these sources are derived from a different population.

Our LFs demonstrate that the UV-bright populations in M 31 and M 32 are not dominated by PAGB stars (assuming that they are free of strong circumstellar extinction). If all of the UV-bright stars were following PAGB tracks, we would expect to observe bright peaks in the luminosity function, well above our detection limits; instead, we see LFs that rise sharply and monotonically at decreasing luminosity. For example, we show in Figure 10 synthetic luminosity functions for a population of stars entering a low-mass ($0.569 M_{\odot}$) PAGB track and an intermediate-mass ($0.633 M_{\odot}$) PAGB track (Vassiliadis & Wood 1994) at the maximum rate allowed in the center of M 31 under the fuel consumption theorem. For old stellar populations (age $\geq 10^{10}$ yr), the number of stars evolving through any evolutionary phase cannot exceed 2.2×10^{-11} stars $L_{\odot}^{-1} \text{ yr}^{-1}$ (Greggio & Renzini 1990). We compute the bolometric luminosity in a given aperture by measuring the F555W *WFPC2* flux, correcting for the 0.06 mag color offset between the F555W filter and the Johnson *V* band, and using a bolometric correction (BC) of -1.25 . This BC is consistent with a stellar population of age 12 Gyr and $[\text{Fe}/\text{H}] = 0.25$ (Worthey 1994), and was chosen on the assumption that the centers of M 31 and M 32 are dominated by old, metal-rich populations. Younger populations would have a smaller BC (e.g., -1.13 for an age of 8 Gyr), as would populations with less metallicity (e.g., -0.96 for $[\text{Fe}/\text{H}] = 0.0$), but these effects are not very significant for our purposes here. The magnitudes in each band are computed with the IRAF package SYNPHOT, using appropriately reddened and normalized Kurucz (1992) synthetic spectra. The PAGB tracks begin after the thermally pulsing (TP) phase, at $T_{\text{eff}} = 10000$ K, and so miss the UV-faint contribution from the rapid evolution up the AGB and through the TP, but qualita-

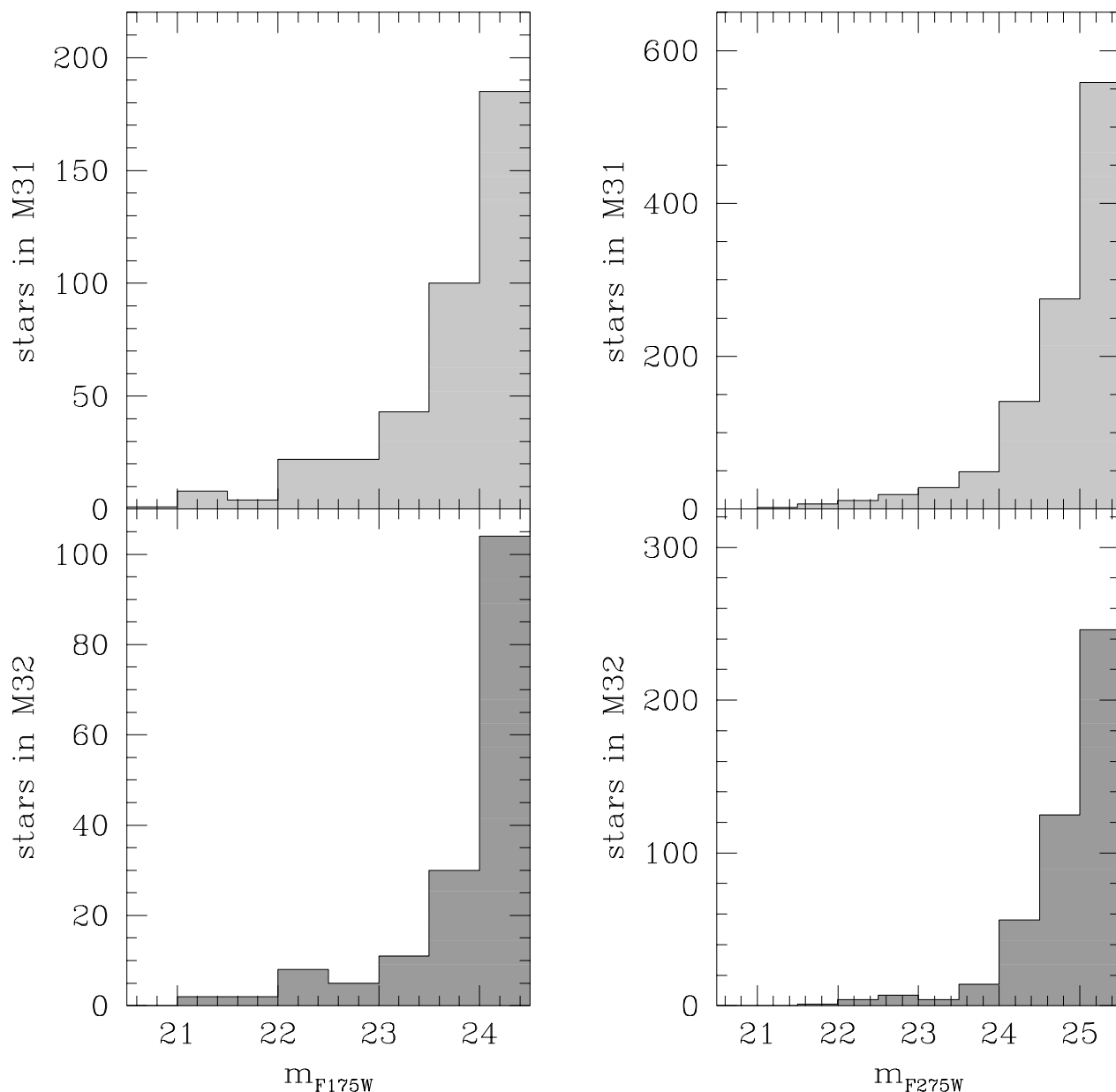


FIG. 9.— The raw luminosity functions for each image shows that the LFs for M 31 (upper panels) look similar to the LFs for M 32 (lower panels). These luminosity functions have not been corrected for completeness and spurious source contamination, because these characteristics are the same for each galaxy in a given band. The luminosity function for a given band only draws upon those sources in the catalog that were detected in that band. The LF for a given band also includes those stars not found in our catalogs that were fainter than the detection limit in the other band. Note that the scale in the M 32 luminosity functions is half that in the M 31 luminosity functions.

tively the LFs should be valid. Circumstellar reddening in the early phases of PAGB evolution could alter the appearance of a PAGB-dominated LF if the stars are hidden behind dust shells during their earliest and brightest phases (see §5.4). Figure 10 also demonstrates that only a dozen or so intermediate-mass PAGB stars could be detected in our M 31 images, while approximately 100 longer-lived low-mass PAGB stars could be detected in these images. The stellar population in M 31 and

M 32 cannot be dominated by low-mass PAGB stars, because they would be detected in significant numbers in our images, unless these stars are hidden by circumstellar extinction (see §5.4). More massive PAGB stars ($\geq 0.633 M_{\odot}$) could dominate the stellar population in these galaxies but not that fraction of the population *above our detection limits*, because they rapidly evolve through their brightest phases. We stress this distinction between PAGB domination of the detected UV-bright popula-

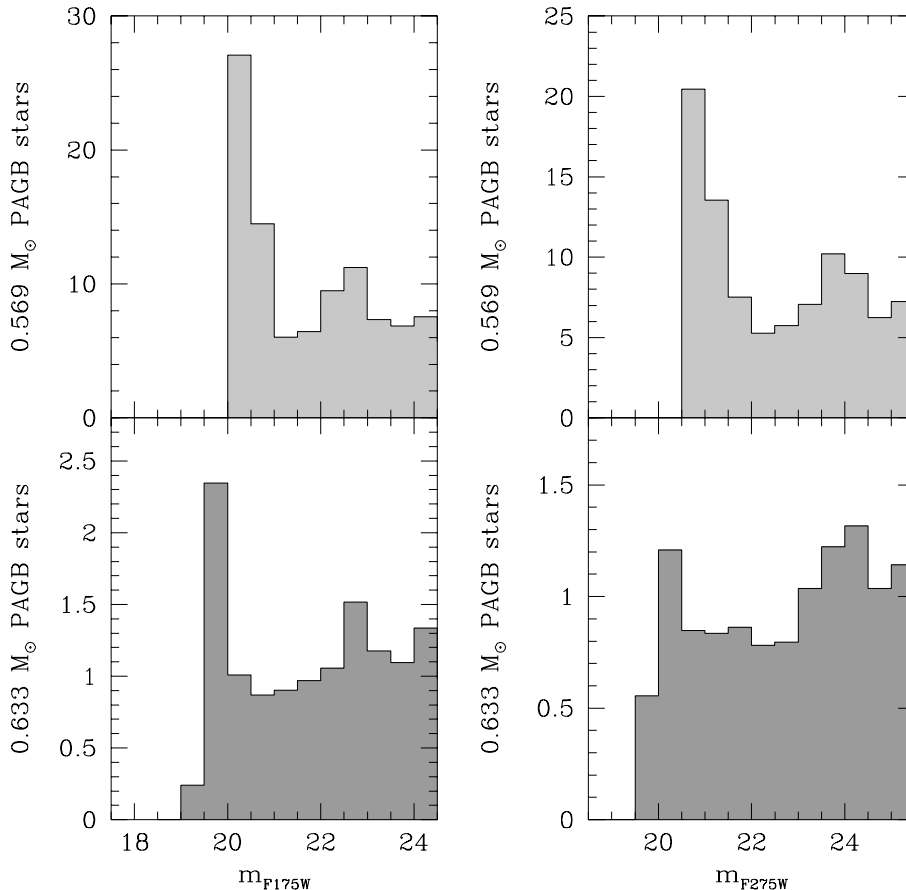


FIG. 10.— The luminosity functions for stars entering a $0.569 M_{\odot}$ PAGB track (top panels) and a $0.633 M_{\odot}$ PAGB track (bottom panels) show that PAGB stars are not the dominant component to the populations detected in our *FOC* images. The scaling was chosen to match the population size allowed under the fuel consumption theorem in the center of M 31; the $0.633 M_{\odot}$ stars evolve more rapidly and so fewer would be found above our detection limits at a given evolutionary rate. The characteristic shape of these LFs (flatter than we observed, with peaks significantly above our detection limits) would be easily detected in the M 31 and M 32 data, implying that our detected UV sources are not dominated by PAGB stars.

tion, and PAGB domination of the *entire* population, which is certainly plausible (and indeed likely, as explained in §5.3). A survey using a wider field of view, perhaps with *STIS*, would be able to detect intermediate-mass ($0.633 M_{\odot}$) PAGB stars if the survey reached as deep as our *FOC* data; for example, given a program that sampled a $100 \times 100''$ field, 296 PAGB stars would be detected in M 31 and 52 would be detected in M 32.

4.3. Color Magnitude Diagrams

We plot the color-magnitude diagrams for M 31 and M 32 in Figures 11 and 12. In each figure, we also plot the evolutionary tracks of Dorman, Rood, & O’Connell, (1993) for solar-metallicity post-EHB stars (0.471 – $0.520 M_{\odot}$) and the evolutionary tracks of Vassiliadis & Wood (1994) for solar-metallicity H-burning PAGB tracks (0.569 – $0.900 M_{\odot}$). The AGB evolution prior to the Vassiliadis & Wood tracks is not shown, due to uncertainties in the thermally pulsing phase and mass loss on the AGB. Although we plot all sources down to $m_{F175W} = 25.5$ mag, the thick black line denotes the limiting magnitudes as determined in §3.4. The errors for a star of a given magnitude vary depending upon the local sky back-

ground, and so we show average 1σ error bars as a function of photometric magnitude. The hottest EHB track ($0.471 M_{\odot}$) plotted has an envelope mass of $0.002 M_{\odot}$, and at its brightest is too faint to be detected in our *FOC* images. Stars of lower envelope mass are possible and are detected in the Galactic field (cf. Mitchell et al. 1998 and references therein), but were not included in the models of Dorman et al. (1993) due to computational limitations.

The *FOC* magnitudes in the tracks are computed by taking the closest Kurucz (1992) synthetic spectrum for the given evolutionary track step, correcting the absolute flux level to account for the mismatch in temperature and gravity between the Kurucz grid and the evolutionary track, applying reddening (Cardelli, Clayton, & Mathis 1989) due to extinction in our own Galaxy (see Table 1), normalizing as appropriate to the distance (see Table 1), and then running the IRAF STSDAS package SYNPHOT. We note that the extinction is a large source of uncertainty in our analysis. For the foreground extinction due to reddening in our own Galaxy, values in the literature vary from $0.035 \leq E(B-V) \leq 0.11$ mag (Tully 1988; McClure & Racine 1969; Burstein et al. 1988; Ferguson & Davidsen

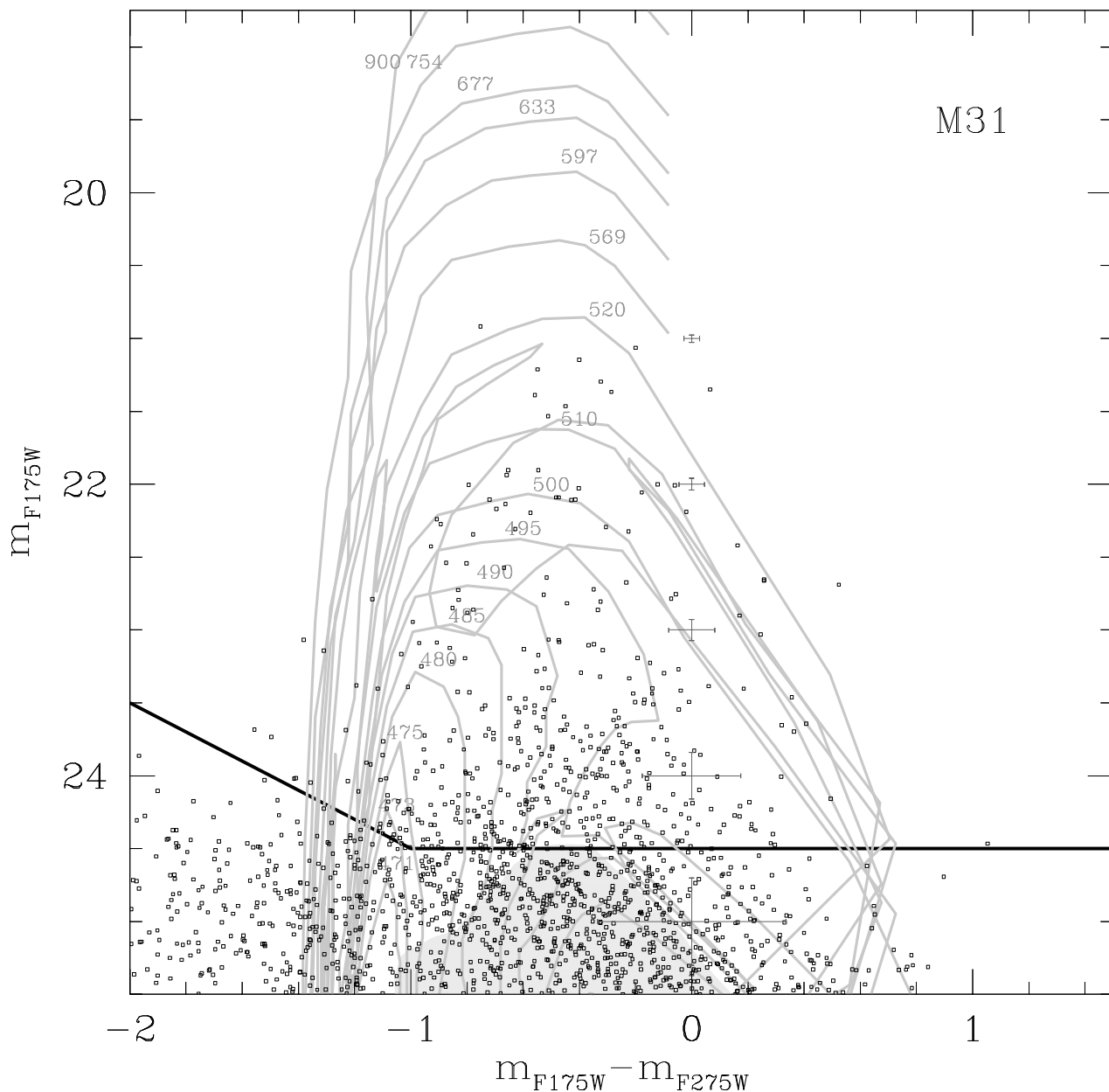


FIG. 11.— The color-magnitude diagram for M 31 shows stars (boxes) arising from a broad distribution of masses (labels) on the HB. The post-EHB evolutionary paths from Dorman et al. (1993) and the PAGB paths of Vassiliadis & Wood (1994) are plotted in light grey. Stars should avoid the shaded region where the evolution is relatively rapid, but this region falls below our limiting magnitudes (solid black line) and is also blurred out by the large statistical uncertainty (error bars) for these faint magnitudes. The AGB is not shown due to uncertainties in the mass loss on the AGB and in the thermally pulsing stage at the end of the AGB.

1993; Burstein & Heiles 1984). Furthermore, internal extinction in the centers of M 31 and M 32 is certainly plausible (cf. Bianchi et al. 1996 and Ciardullo et al. 1988), and may even be patchy in the center of M 31. A fraction of these stars may also have circumstellar extinction from dust shells ejected during their evolution (e.g., as planetary nebulae); the timescale for the “thinning” of such circumstellar extinction (at least in the optical bands) is very uncertain. We explore PAGB circumstellar extinction in §5.4.

The most important aspect to note about this diagram is that the tracks leaving the blue extreme of the horizontal branch appear to be populated. These post-EHB stars are the same hot subdwarfs seen in our own Galactic field, and our *FOC* images represent the first time these stars have been directly detected outside of our own Galaxy.

As stars evolve from the HB and toward eventual death on the white dwarf cooling track, they spend the longest fraction of time on the HB itself (note that the HB falls below the bot-

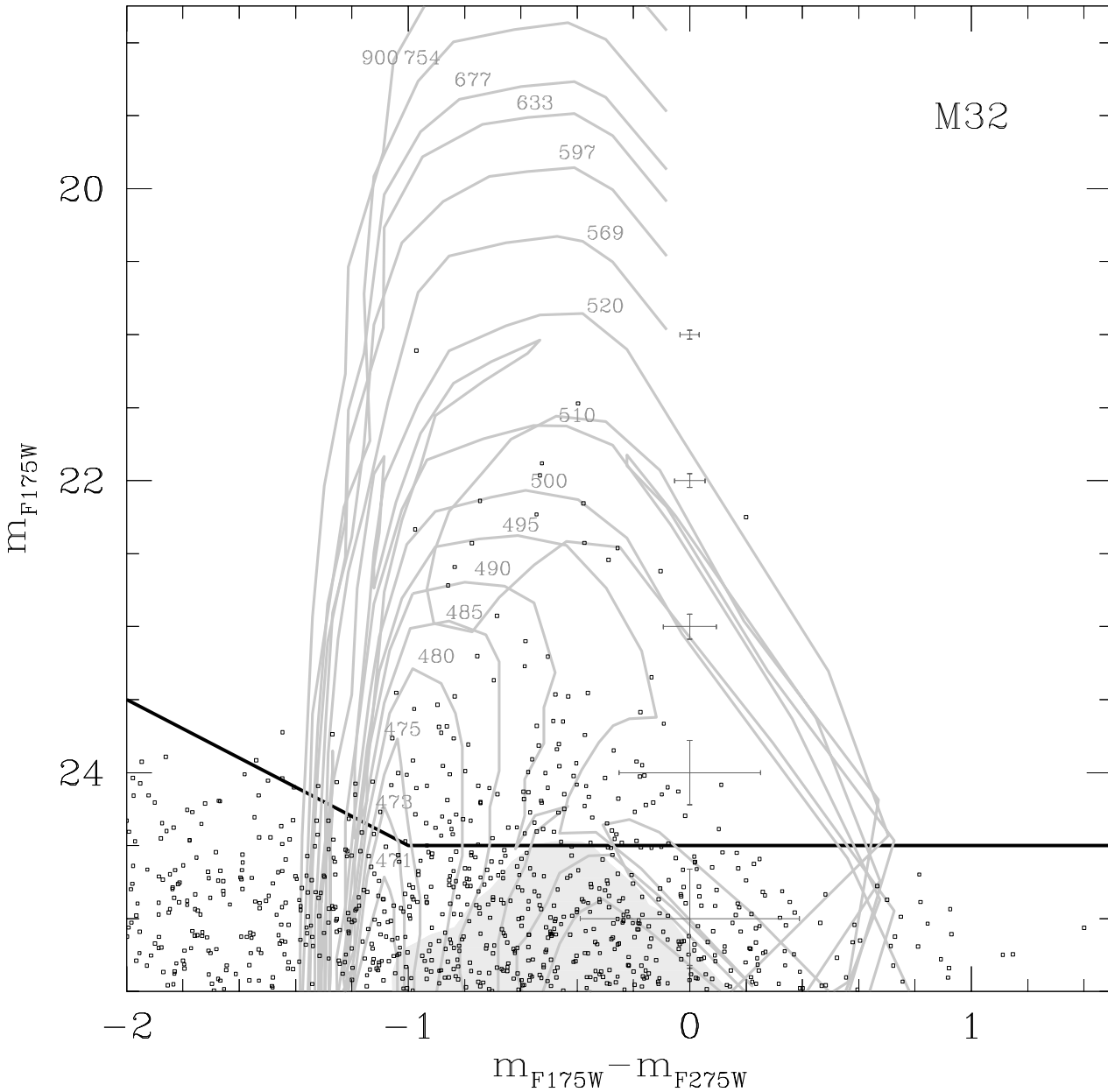


FIG. 12.— The color-magnitude diagram for M 32 appears very similar to the M 31 CMD (Figure 11). The only notable distinctions here are the fewer number of stars and the lack of red stars.

tom of Figures 11 & 12). Upon core helium exhaustion, stars will either ascend the AGB (not shown in the figures) or one of the post-EHB tracks (following either AGB-Manqué or post-early-AGB behavior). The evolution upon leaving the HB is relatively rapid, but then slows down again, before proceeding to the white dwarf cooling curve. Thus, a gap should appear in a CMD of post-HB stars. We show this gap as a shaded region in Figures 11 and 12; it is obvious in population simulations (cf. §5.2 and Figure 15). Unfortunately, our CMDs do not reach deep enough to detect this gap; most of the stars below the thick black line in the figures are either spurious sources or have large statistical uncertainties, thus blurring any gap if

present.

Because these evolved stars spend the vast majority of their time on the HB before proceeding to their later phases, we are resolving only a small fraction of the UV flux in these CMDs (as discussed in §5.3). For every star we detect in the relatively rapid post-HB phases, there are many more sitting on the horizontal branch. Until a CMD extends to the HB, most of the UV flux in these galaxies will remain unresolved.

Main sequence stars or blue stragglers are unlikely contributors to the population shown in our CMDs. In Figure 13, we show the M 31 CMD, but now plot the main sequence instead of post-HB stars. The zero-age main sequence (ZAMS) is com-

puted from solar-metallicity tracks of Bressan et al. (1993), and is labeled with the masses of the stars at selected points. Although the main sequence passes through the population of detected stars, our detected stars do not appear to be clumping around the ZAMS. This is in line with expectations, because stars of such high mass would be extremely young; the approximate turnoff ages corresponding to each of the masses in the diagram are: 25 Myr ($9 M_{\odot}$), 40 Myr ($7 M_{\odot}$), 50 Myr ($6 M_{\odot}$), 80 Myr ($5 M_{\odot}$), 125 Myr ($4 M_{\odot}$), and 250 Myr ($3 M_{\odot}$). Although the stars near the detection limit could possibly be 250 Myr old main sequence stars, it seems implausible that star formation stopped so recently and abruptly in M 31 and M 32. Blue stragglers, the possible result of binary mergers, could conceivably contribute at the detection limits, because a $3 M_{\odot}$ blue straggler could be the product of two $1.5 M_{\odot}$ stars of 2 Gyr age, but brighter than these limits their contribution becomes less plausible.

Figures 11 and 12 show what may be a few fading PAGB stars along the left hand side of the diagram. Such stars may show significant emission lines from any surrounding planetary nebulae, and we note that the stellar spectra used to trace the tracks in the CMDs do not account for such emission lines. The presence of strong lines would tend to move the stars to the left (blue) and up (brighter) in the CMDs, because the strongest lines fall well within the F175W bandpass. For example, in the well-studied planetary nebula NGC 7662, the line strengths of C IV $\lambda 1549$ and C III] $\lambda 1908$ relative to [O III] $\lambda 5007$ are observed to be 0.553 and 0.289, respectively (Osterbrock 1989). Ciardullo et al. (1989) measured [O III] $\lambda 5007$ for planetary nebulae in the M 31 bulge to have a range of $20.31 \leq m_{5007} \leq 24.53$ mag, translating to $2.40 \times 10^{-14} \geq F_{5007} \geq 4.92 \times 10^{-16}$ erg cm $^{-2}$ s $^{-1}$. If for the purposes of demonstration we take the brightest [O III] flux, compute the intensities in C III] and C IV (accounting for the reddening in M 31), and run these fluxes through SYNPHOT, we find that a $T_{\text{eff}} = 108000$ K PAGB star ($0.633 M_{\odot}$) would move significantly in the M 31 CMD. Without the emission lines, $m_{F175W} = 23.10$ mag and $m_{F175W} - m_{F275W} = -1.29$ mag, but with the emission lines, these would change to $m_{F175W} = 21.22$ mag and $m_{F175W} - m_{F275W} = -3.03$ mag.

As was the case with the luminosity functions in §4.2, there do not appear to be any dramatic differences between the evolved stellar populations of M 31 and M 32 seen in our CMDs. The stars are for the most part evenly distributed among the post-HB tracks in both galaxies. The only significant difference (other than the larger number of stars seen in the M 31 CMD) might be the appearance of a greater “red” post-HB population in M 31.

The statistical uncertainty for the magnitudes of most stars in our CMDs is large enough to cause considerable “blurring” of the CMDs. For this reason alone, it would not be feasible to fit the mass distribution for the horizontal branches of M 31 and M 32. However, the many systematic uncertainties also prevent a more precise characterization at this time. The dominant uncertainty is the reddening applied to the tracks (see above). The stars would shift 0.24 mag to the right or upward in the CMDs if the F275W filter or both filters are not correctly calibrated (see §3.3). There are theoretical uncertainties in the evolutionary tracks themselves. For these reasons, we must limit the conclusions we draw regarding these populations. The stars shown in our CMDs can be characterized, as a whole and with considerable certainty, to be evolving from the EHB, but we cannot use

the distribution of stars in the CMDs to determine the distribution of mass for the horizontal branch progenitors.

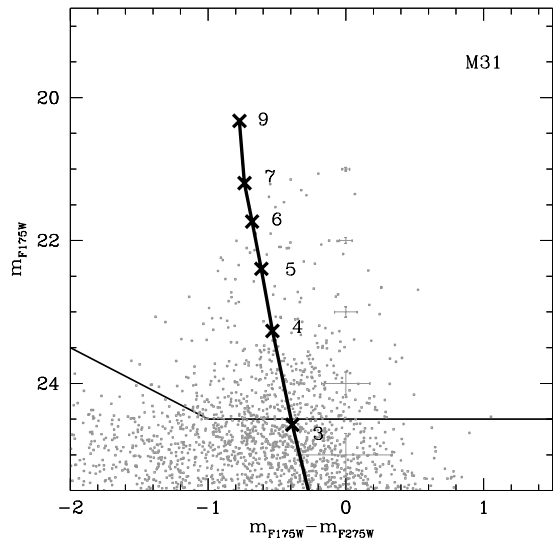


FIG. 13— The CMD for M 31 (cf. Fig. 11), but instead of post-HB tracks, the zero-age main sequence (ZAMS) is plotted for a range of masses appropriate to the luminosity and temperature of this population, assuming solar-metallicity and a reddening of $E(B-V) = 0.11$ mag. The masses of the ZAMS stars are labeled in solar units. Note that only very recent star formation could populate this portion of the ZAMS. The stars do not appear to be clumping near the ZAMS (or along any line shifted with respect to the ZAMS), even where the photometric errors are small.

5. MODELLING

5.1. EHB Luminosity Function

From the spectral-synthesis results of Ferguson & Davidsen (1993) and Brown et al. (1997), we expect that the LFs are dominated by post-EHB stars, i.e., AGB-Manqué stars and PEAGB stars (Greggio & Renzini 1990). Due to the limitations imposed by the observational uncertainties, detailed fitting of the EHB mass distribution does not seem warranted. Furthermore, there exist no a priori predictions of the HB mass distribution. However, we can explore the simple test case of a flat distribution of mass (i.e., a constant number of stars per year per unit EHB star mass joining the zero-age HB), and compare to the FOC data, in order to see if the populations characterized in the data are consistent with a population of EHB stars. Although the EHB tracks appear to be populated (see §4.3), a simulation properly accounts for the timescales in the evolutionary tracks; slower phases should be more populated than faster phases of post-HB evolution, and such subtleties are not obvious to the eye in a CMD.

A flat distribution of mass on the EHB reproduces the measured luminosity functions reasonably well. In Figure 14 we show the LFs we obtain from a population evolving from a uniform distribution of mass on the extreme horizontal branch ($0.471\text{--}0.530 M_{\odot}$), scaled so that the number of stars above our detection limits matches that seen in M 31. For this simulation, we use the evolutionary tracks of Dorman et al. (1993); the magnitudes are derived using SYNPHOT with Kurucz synthetic spectra. The top panels show the LFs from the test population as we would measure them all the way down to the horizontal

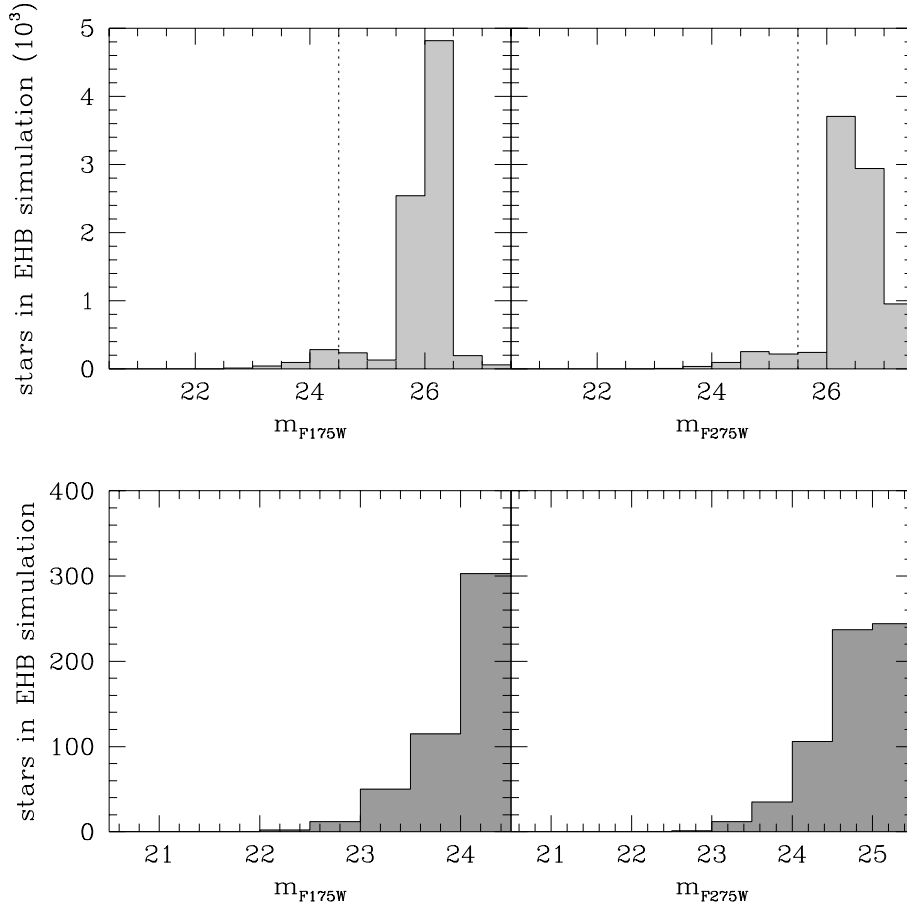


FIG. 14.— The luminosity function for stars entering EHB tracks of mass $0.471\text{--}0.530 M_{\odot}$, normalized to reproduce the number of stars found above the detection limits in the M 31 images. In the top panels, the luminosity functions do not account for photometric statistical errors, and are shown all the way down to the HB (dotted lines denote our actual limiting magnitude in each band). In the bottom panels, the LFs include photometric errors, and are shown on the same scale as Figure 9. Although these LFs agree with Figure 9 better than the PAGB LFs in Figure 10, the actual F275W LF in M 31 includes more faint red stars than predicted by such a simple model.

branch without photometric uncertainties, and the bottom panels show the LFs on the same horizontal scale as the measured LFs in Figure 9, including the effects of photometric uncertainties. The major difference between the simulated LFs in Figure 14 and the actual M 31 LFs in Figure 9 is that the measured F275W LF peaks higher than the measured F175W LF, whereas the simulated LFs peak at approximately the same height in each band. The measured LFs thus show a redder population than the simulated EHB LFs. However, the simulated flat EHB population in Figure 14 shows much better agreement with the measured LFs (Figure 9) than a PAGB-dominated LF (Figure 10).

5.2. EHB Color Magnitude Diagram

For comparison to the actual CMDs (Figures 11 and 12), we can simulate the CMD we would expect for this flat EHB mass distribution, again using the evolutionary tracks for these stars (Dorman et al. 1993). The simulation is shown in Figure 15. Although they comprise the majority of the population below the detection limits, PAGB stars are not included in the simulation, due to uncertainties along the AGB and in the ther-

mally pulsing phase. In the simulation, the total number of stars brighter than our detection limits in each band matches the number of stars detected above these limits in M 31. The top panel shows the simulation without statistical errors; in the bottom panel, random noise in the colors and magnitudes has been added to the simulation, assuming the same data quality seen in the M 31 observation. We note that the bottom panel does not take into account the increase in spurious sources and decrease in completeness as one approaches our detection limits. The bottom panel in the simulation appears similar to the CMD seen in M 31 (Figure 11), given that the simulation is meant to demonstrate a zeroth order model as an example.

A quantitative comparison of the simulated population (Figure 15b) to the M 31 population (Figure 11) is shown in Figure 16. The figure partitions the CMDs into regions that span 0.5 mag in color and 1 mag in luminosity; such partitioning is appropriate given systematic errors smaller than 0.3 mag. In each region we have denoted the number of stars in the M 31 CMD (bold) and the number of stars in the simulation (italics). It is clear that overall, the flat distribution of EHB stars shown in the simulation produces a population that is highly concentrated

toward the lower central regions of the CMD, as seen in M 31. The M 31 CMD shows a few more red stars along the right hand side, and a few less blue stars along the left hand side. The significant difference, however, is that the M 31 CMD shows considerably more stars brighter than $m_{F175W} = 22.5$ mag, as compared to the simulation. The difference is large enough to imply a contribution to the population in M 31 that is lacking in the simulation.

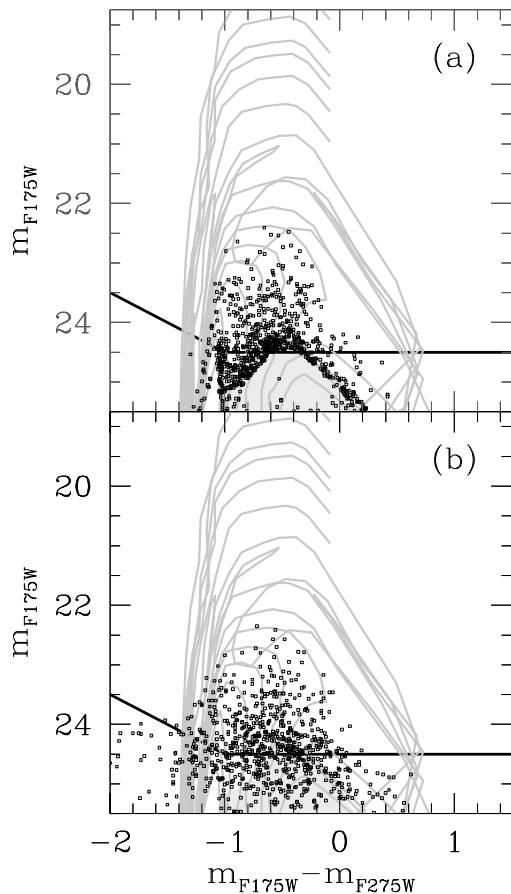


FIG. 15— This simulated CMD results from a uniformly populated EHB (with ZAHB mass of $0.471\text{--}0.530 M_{\odot}$), but no contribution from the red HB that gives rise to the PAGB stars. The number of stars in the simulation above the detection limits (black line) matches the same number detected in M 31 (Fig. 11). The top panel shows the simulation without noise (note the avoidance of the shaded region); the bottom panel reflects the statistical errors found in the M 31 data.

What are these brighter stars? The simplest way to populate that portion of the CMD is with post-early-AGB stars. Such stars evolve from the EHB along the AGB, but leave the AGB before the thermally pulsing phase. On the zero-age horizontal branch, they are cooler and more massive than the stars that evolve into AGB-Manqué stars. PEAGB stars are likely to originate as stars with masses of $0.51\text{--}0.55 M_{\odot}$ on the ZAHB. While such stars are present in our simple model, they are evidently not present in sufficient numbers.

However, we find that it is not possible to increase the number of PEAGB stars without considerably worsening the agreement with the far-UV spectrum. To match the counts in the bright portion of the CMD, the population of PEAGB stars

would have to be increased by a factor of ~ 100 . However this additional population would make the M 31 integrated spectrum three times brighter and significantly cooler than actually observed by *HUT*. Thus, we consider it unlikely that the very brightest stars in the M 31 CMD are PEAGB stars. It also seems unlikely that these stars are merely the result of crowding, given the modest number of resolved stars in our M 31 images, and the existence of such stars even near the edges of our fields. Thus the nature of the $m_{F175W} < 22.5$ population is a bit of a puzzle. Testing other hypotheses (e.g. reddened PAGB stars, binary AGB-Manqué stars, or accreting white dwarfs) is beyond the scope of this paper, but appears to be an interesting avenue for further investigation.

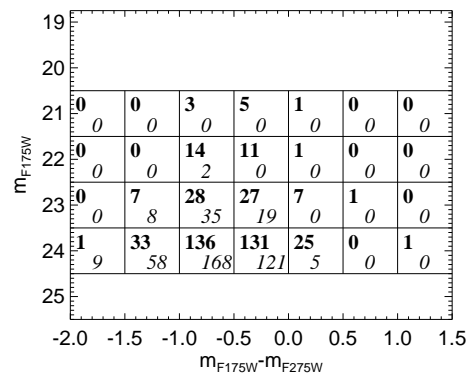


FIG. 16— A quantitative comparison of the CMDs shown in Figures 11 and 15b shows good agreement in general but notable discrepancies. The number of stars per $0.5 \text{ mag} \times 1.0 \text{ mag}$ region in the M 31 CMD is shown in bold, while that number in the EHB simulation is shown in italics. The M 31 population and the simulated EHB population both show a strong concentration toward the faint center. However, there are ~ 30 stars at $m_{F175W} \geq 22.5$ mag in the M 31 CMD that are not present in the simulated CMD.

5.3. Comparison to Expectations from *IUE* and *HUT*

How much of the *IUE* flux do we resolve into stars? Does the *FOC* flux (both diffuse and stellar) agree with the expectations from *HUT* and *IUE*? In §3.3.2, we compared the *IUE*+Optical flux to the *FOC* and *WFPC2* flux within $1.4''$ of the galaxy centers, in order to minimize uncertainties in the sky and dark count background while investigating any systematic errors in the *FOC* calibration. Here, we compare the *FOC* flux in the full *IUE* aperture to expectations from the *IUE*+Optical spectrum, and compare the stellar light to expectations from both *IUE* and *HUT*.

Because the $10 \times 20''$ oval *IUE* aperture is larger than the $14 \times 14''$ *FOC* field, we have defined two regions (see Figures 4 and 5) in the *FOC* field for comparison to the *IUE* flux. Region “A” is centered on the nucleus in each galaxy, and region “B” runs from “A” to a distance of $10''$ from the galaxy center. The regions are defined such that $A+2B$ is equivalent to the *IUE* aperture, given approximate symmetry in the galaxies about their centers.

The net *FOC* count rate within the *IUE* aperture is shown in Table 6 (row 4), and is the result of subtracting the expected sky count rate (row 3) and expected dark count rate (row 2) from the gross count rate (row 1). We again assume a high sky background, although unlike our calculations in §3.4 and

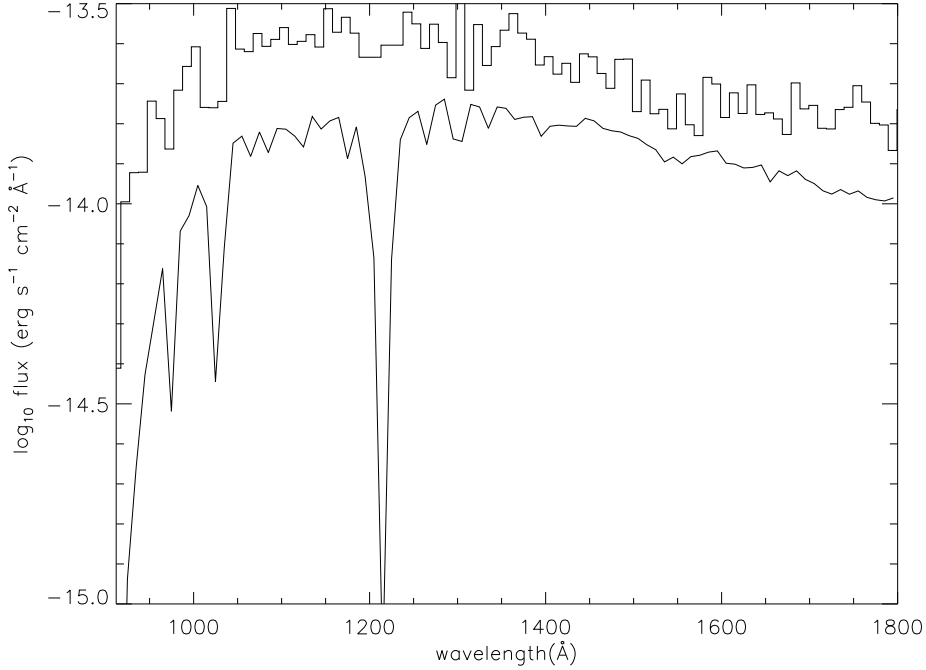


FIG. 17— The *HUT* spectrum of M 31 (histogram; binned to 10 Å) shown with the spectrum we would obtain from a two-component population of evolved stars: a flat distribution of EHB stars, and a population of $0.633 M_{\odot}$ PAGB stars. The number of EHB stars was chosen to match the number above the detection limits in the M 31 images, and the number of PAGB stars was chosen to match that allowed under fuel consumption constraints (accounting for the small contribution from the EHB stars); the entire model was then multiplied by 3.59 to account for the aperture difference between the *FOC* stellar sample and the *HUT* $9.4 \times 116''$ slit.

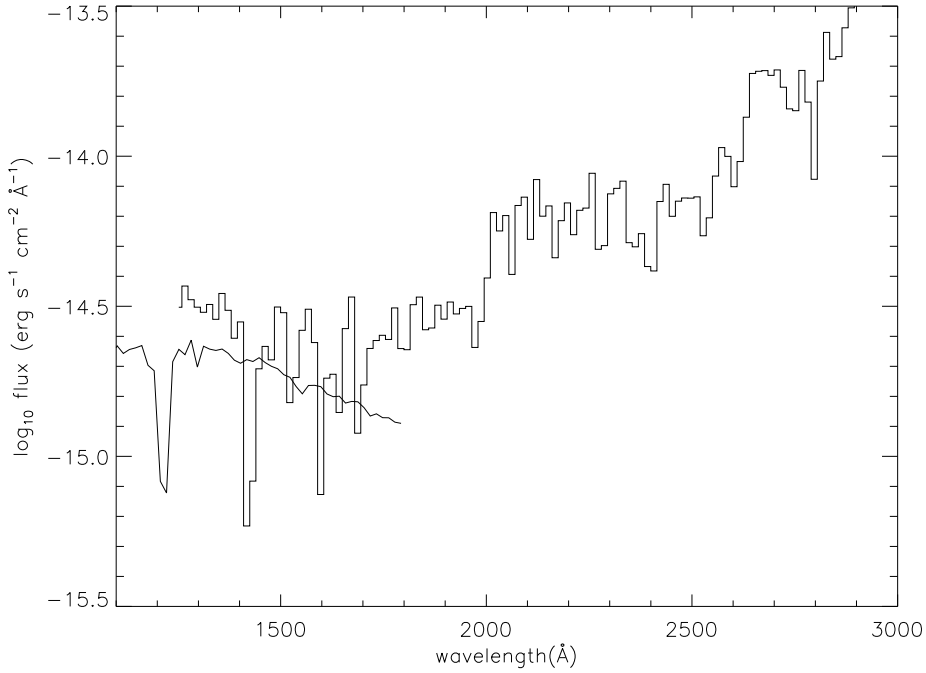


FIG. 18— The *IUE* spectrum of M 32 (histogram; binned to 15 Å) shown with the spectrum we would obtain from a two-component population of evolved stars: a flat distribution of EHB stars, and a population of $0.633 M_{\odot}$ PAGB stars. The number of EHB stars was chosen to match the number found above the detection limits in the M 32 images, within the region “A” plus twice that number found in region “B” (cf. Figure 5), thus accounting for the difference between the *FOC* and *IUE* apertures. The number of PAGB stars was chosen to match that allowed under fuel consumption constraints (accounting for the small contribution from the EHB stars).

Table 5, the sky and dark background contribute significantly to the flux within this large area. Running the composite *IUE*+Optical spectrum through the IRAF package SYNPHOT gives the predicted flux within the *IUE* aperture (row 6), and a comparison (row 8) of this expectation with our measurement shows that our *FOC* F175W images detect more flux than predicted from *IUE*, while the F275W images detect less flux than predicted. Given the uncertainty in the dark and sky background for the *FOC*, we can say that the flux measured by the *FOC* cameras roughly agrees with the predictions made from the *IUE*+Optical composite spectrum.

To compare to the flux in resolved sources, we limit ourselves to those stars that are above our limiting magnitudes (i.e., $m_{F275W} < 25.5$ mag and $m_{F175W} < 24.5$ mag). We compare the flux from the stars found in the *IUE* “aperture” (again regions A+2B) to the UV flux seen by *IUE*. We define the UV flux in the F175W filter to be that flux shortward of 2400 Å, and the UV flux in the F275W filter to be that flux shortward of 3400 Å; flux longward of these wavelengths is considered “red leak” in the filters. As the numbers in Table 6 demonstrate, the F175W filter suffers from a very high red leak, while the F275W filter shows a moderate contribution from red leak photons. The high percentage of red leak in these calculations is due to the fact that both galaxies are very red and emit much more light at longer wavelengths than in the UV when integrating over a synthesized $10 \times 20''$ aperture; we note that the percentage of red leak in the light from hot stars is far less important. For example, for *FOC* photometry of a 20000 K star in M 31 or M 32, the red leak contribution to the measured light is less than 12% in F175W and less than 3% in F275W. If we assume that the stars above our limiting magnitudes emit the bulk of their flux in the UV, it is reasonable to compare (row 9) the counts found in these stars to the UV count rate predicted from *IUE*. The UV flux from our resolved hot stars only accounts for a small fraction (<20%) of the UV light observed with *IUE*. This result is understood if we trace these post-HB stars back to their HB progenitors.

As we did in Sections 5.1 and 5.2, we again use a flat distribution of stars on the EHB and its post-HB descendents, and then scale this population so as to reproduce the number of stars found above our detection limits in M 31 and M 32. Note that many more stars in this model are below the detection limits than above (see Figure 14). We then add a $0.633 M_{\odot}$ PAGB component, with the number of stars scaled to match the limits allowed under the fuel consumption theorem (taking into account the small contribution from the EHB stars). Because the UV-bright phase of these PAGB stars is so short-lived, only a dozen or so would appear in each of the M 31 and M 32 images (see Figure 10). We then use the spectral library of Brown, Ferguson, & Davidsen (1996) to compute the integrated spectra of these populations, and compare to the actual far-UV spectra of M 31 and M 32 as measured by *HUT* and *IUE* respectively. These comparisons are shown in Figures 17 and 18. Note that the model spectrum in each figure has been rescaled to match the flux expected in the *HUT* and *IUE* apertures, but has not been renormalized otherwise. The disagreements between the model and the observed spectra are thus real and due either to a failure of this aperture correction to match the true UV profile of the galaxies, or a missing UV population in the model.

The figures demonstrate that most of the unresolved flux in M 31 and M 32 can be explained, once we trace back the bright post-HB population detected in the *FOC* to its HB progenitors.

Given the large uncertainty in the aperture matching between the *FOC*, *HUT*, and *IUE*, the agreement between the model spectrum and the far-UV data is good. For M 31, a model population that reproduces the number of detected stars and the UV light has 98% of its main sequence stars evolving into PAGB stars, and only 2% into EHB stars (with a flat mass distribution). For M 32, a model that reproduces the number of detected stars and the UV light has 99.5% of its main sequence stars evolving into PAGB stars and 0.5% into EHB stars. The far slower evolution of the EHB stars more than compensates for the smaller number of their progenitors relative to those for the PAGB stars. The smaller fraction of resolved UV flux in M 32 is explained by a smaller fraction of stars following the longer-lived EHB evolutionary paths. Although the uncertainties are large, the model spectrum in each galaxy falls a bit short of those measured by *HUT* and *IUE*, and the discrepancy is largest at the shortest wavelengths. Very hot EHB stars (and their descendants), with envelope mass less than $0.002 M_{\odot}$, could be present and make significant contributions to the far-UV flux in these galaxies. These stars are just below our detection limits, even in their brightest phases, as we discuss in §4.3.

5.4. PAGB Circumstellar Extinction

We demonstrated in §4.2 that the luminosity functions in M 31 and M 32 do not appear to be dominated by PAGB stars. Nor do the PAGB tracks in the color magnitude diagrams (§4.3 and Figures 11 and 12) appear to be populated. Our analysis showed that a dominant population of low-mass ($0.569 M_{\odot}$) PAGB stars would produce many detections in our *FOC* images, because of their relatively slow evolution through the earlier bright phases, while a dominant population of intermediate-mass PAGB stars ($0.633 M_{\odot}$) stars would produce a negligible number of detections due to more rapid evolution. Given a population that is dominated by PAGB stars (see §5.3), our data implies that either the PAGB stars are of intermediate mass (or greater), or that they are low-mass stars hidden by circumstellar extinction during their early bright phases. In this section we explore the latter case.

Käuffl, Renzini, & Stanghellini (1993) derived a simple model for circumstellar extinction in PAGB stars. This extinction would be caused by the shell of material expelled on the AGB during the “superwind” phase. The initially opaque shell would begin thinning with the end of the superwind phase, as it expands outward from the underlying star. Käuffl et al. computed the “thinning time” for this shell to become transparent at $H\alpha$ and $Br\alpha$. We can also apply the Käuffl et al. model to see the maximum effect of such an expanding shell in the far-UV. Of the 7 models considered by Käuffl et al. (1993), the one with the strongest and most prolonged extinction in the far-UV is Model 1, having a superwind mass loss rate of $10^{-3} M_{\odot} \text{ yr}^{-1}$, grain size $0.1 \mu\text{m}$, expansion velocity 10 km s^{-1} , and superwind duration 10^3 yr . The absorption coefficient for $0.1 \mu\text{m}$ grains is respectively 1.348 and 0.413 at 1750 and 2750 Å Draine & Lee (1984). The time at which the superwind phase ends is uncertain, but is thought to occur somewhere around an effective temperature of 5000–7000 K, on or near the AGB (Käuffl et al. 1993; Vassiliadis & Wood 1994). Because we are investigating the maximum effect of such a shell, we shall choose to quench the superwind immediately prior to the start of the PAGB tracks (cf. Figures 11 and 12), at 10000 K, thus prolonging the thinning as far possible into the UV-bright phase of the PAGB evolution.

We demonstrate the effect of such circumstellar (CS) extinc-

tion on the low-mass ($0.569 M_{\odot}$) PAGB track. We found in §4.2 that if the PAGB stars in the M 31 and M 32 cores were following such low-mass tracks, they should be detectable in the *FOC* in significant numbers, as long as CS extinction was not significant. Figure 19 shows m_{F175W} and m_{F275W} as a function of time for such stars, with and without CS extinction. It takes approximately 10000 years for the circumstellar shell to become optically thin at 1750 Å, and 4000 years to become optically thin at 2750 Å. We can see that the luminosity functions we measured in the *FOC* images would still show a bright peak well above our detection limits, even with the CS extinction. A more realistic model would begin the thinning of the shell at time several 10^3 yr earlier, and in such a case the extinction would have a very negligible effect on our data.

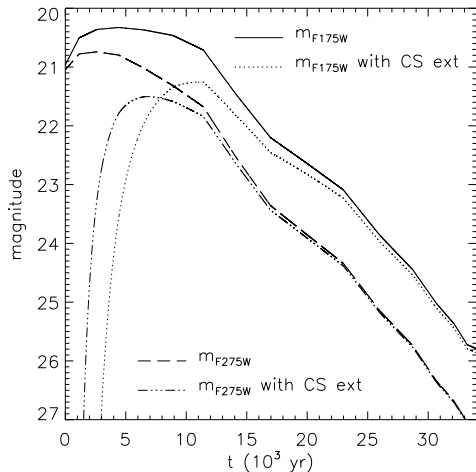


FIG. 19— The evolution of a low-mass ($0.569 M_{\odot}$) PAGB track as observed with and without circumstellar extinction. The CS extinction model has been chosen to maximize the effect in the far-UV, but it would still not significantly affect the detection of such low-mass PAGB stars in the *FOC* field. Intermediate-mass PAGB stars are thus more likely to dominate the populations in M 31 and M 32.

6. DISCUSSION

Since the discovery of the UV upturn phenomenon, a great deal of research has tried to characterize the stellar population producing the UV light in spiral bulges and ellipticals. The range of candidates has included young massive stars, hot horizontal branch stars, planetary nebula nuclei (PAGB stars), and several binary scenarios (see Greggio & Renzini 1990 for a complete review). Earlier work relied primarily upon *IUE* and *HUT* spectra of composite stellar populations, and pre-COSTAR *FOC* observations (King et al. 1992; Bertola et al. 1995) of the brightest stars. Our current understanding of the populations in ellipticals and spiral bulges predicts that a significant population of hot HB and post-HB stars should be evolving from the extreme horizontal branch and following either AGB-Manqué or post-early-AGB evolution (see Brown et al. 1997 and references therein). The prediction is mainly based upon fuel consumption constraints that rule out PAGB stars as the sole UV producers; the PAGB stars are just too short-lived to efficiently produce the required UV light.

Our *FOC* observations confirm the existence of hot post-EHB stars in the centers of M 31 and M 32, and also confirm that PAGB stars are not the predominant component of the UV-

bright population. The existence of these EHB stars also implies that the horizontal branches in both M 31 and M 32 are at least somewhat extended, because “red clump” horizontal branches are unlikely to produce the stars seen in our color-magnitude diagrams. Future observations, given the improved UV capabilities of HST with the installation of *STIS*, should be able to reach the HB and thus characterize the entire evolved population more directly. We note that significant systematic uncertainties may exist in our *FOC* photometry, at the 0.3 mag level. Our results should be considered with these uncertainties in mind; however, the uncertainties are not large enough to allow a completely different interpretation of the detected stellar population.

As discussed in §5.2, we find a minority population ($\sim 10\%$) of brighter stars that cannot be explained by canonical post-HB evolutionary tracks. Although PEAGB or very low-mass PAGB stars evolve through this region of the CMD, their evolution during this phase is too rapid to produce the 35 stars seen in M 31 while maintaining consistency with fuel consumption constraints and observed integrated spectra of M 31. The nature of these stars remains unexplained as of this writing.

The fraction of light in the resolved UV population in the center of M 31 and in the center of M 32 is consistent with expectations from the *HUT* and *IUE* spectra of these galaxies. The far-UV light in M 31 can be explained by a main sequence population where 98% of the stars channel through intermediate-mass PAGB evolution and 2% through EHB evolution. The far-UV light in M 32 can be explained by a population where 99.5% of the stars channel through intermediate-mass PAGB evolution and 0.5% through EHB evolution. Our simple model populations can account for most of the far-UV light, although there is room in both galaxies for a contribution from very low-mass hot EHB stars, which would be below our detection limits even in the AGB-Manqué phase.

We found that the stellar populations in M 31 and M 32 do not appear remarkably different in our *FOC* UV images. Fewer stars appear to be entering the UV-efficient EHB paths in M 32, and this explains both the smaller absolute number of detected stars and the smaller fraction of resolved UV light. The similarities of the luminosity functions of M 31 and M 32 were unexpected, given the dramatically different $m_{1550} - V$ colors of the two galaxies. This finding suggests that, while the fractional mass in EHB stars is probably sensitive to the properties of the overall stellar population, (e.g., metallicity, age, or helium abundance), the mass distribution on the EHB may not be as sensitive to these parameters. Certainly, the differences can not be investigated without deeper images that can resolve more of the evolved population. *STIS* observations planned for late 1998 will reach the HB in M 32 and provide direct evidence for the horizontal branch distribution.

Support for this work was provided by NASA through grant number GO-5435 from the Space Telescope Science Institute, which is operated by the Association of Universities for Research in Astronomy, Incorporated, under NASA contract NAS5-26555. TMB acknowledges support at Johns Hopkins University by NAS 5-27000 and at Goddard Space Flight Center by NAS 5-6499D. The work by SAS at IGPP/LLNL was performed under the auspices of the US Department of Energy under contract W-7405-ENG-48. We wish to thank Robert Jędrzejewski and Ivan King for providing insight into *FOC* calibration issues.

REFERENCES

- Bertola, F., Capaccioli, M., & Oke, J. B. 1982, *ApJ*, 254, 494
- Bertola, F., Bressan, A., Burstein, D., Buson, L. M., Chiosi, C., & Alighieri, S. D. S. 1995, *ApJ*, 438, 694
- Bianchi, L., Clayton, G. C., Bohlin, R. C., Hutchings, J. B., & Massey, P. 1996, *ApJ*, 471, 203
- Bressan, A., Chiosi, C., & Fagotto, F. 1994, *ApJS*, 94, 63
- Bressan, A., Fagotto, F., Bertelli, G., & Chiosi, C. 1993, *A&AS*, 100, 647
- Brocato, E., Matteucci, F., Mazzitelli, I., & Tornambe, A. 1990, *ApJ*, 349, 458
- Brown, T. M., Ferguson, H. C., & Davidsen, A. F. 1996, *ApJ*, 472, 327
- Brown, T. M., Ferguson, H. C., Davidsen, A. F., & Dorman, B. 1997, *ApJ*, 482, 685
- Burstein, D., Bertola, F., Buson, L. M., Faber, S. M., & Lauer, T. R. 1988, *ApJ*, 328, 400
- Burstein, D., & Heiles, C. 1984, *ApJS*, 54, 33
- Cardelli, J. A., Clayton, G. C., & Mathis, J. S. 1989, *ApJ*, 345, 245
- Ciardullo, R., Jacoby, G. H., Ford, H. C., Neill, J. D. 1989, *ApJ*, 53, 69
- Ciardullo, R., Rubin, V. C., Ford, W. K., Jr., Jacoby, G. H., & Ford, H. C. 1988, *AJ*, 95, 438
- Code, A. D., & Welch, G. A. 1979, *ApJ*, 228, 95
- Dorman, B., O'Connell, R. W., & Rood, R. T. 1995, *ApJ*, 442, 105
- Dorman, B., Rood, R. T., & O'Connell, R. W. 1993, *ApJ*, 419, 596 (DRO93)
- Draine, B. T., & Lee, H. M. 1984, *ApJ*, 285, 89
- Ferguson, H. C. et al. 1991, *ApJ*, 382, L69
- Ferguson, H. C., & Davidsen, A. F. 1993, *ApJ*, 408, 92
- González, J. J., & Gorgas, J. 1995, in *ASP Conf. Proc. 86, Fresh Views of Elliptical Galaxies*, ed. A. Buzzoni, A. Renzini, & A. Serrano (San Francisco: ASP) 225
- Greenfield, P. 1994, in *Instrument Science Report FOC-075, Format-Dependent Sensitivity Effects*, http://www.stsci.edu/ftp/instrument_news/FOC/Foc_isr/foc_isr075.ps
- Greggio, L., & Renzini, A. 1990, *ApJ*, 364, 35.
- Holtzman, J. et al. 1995, *PASP*, 107, 156
- Horch, E., Demarque, P., & Pinsonneault, M. 1992, *ApJ*, 388, L53
- Jedrzejewski, R. 1996, in *Instrument Science Report FOC-085, Results of the Cycle 4 FOC DQE Program*, http://www.stsci.edu/ftp/instrument_news/FOC/Foc_isr/foc_isr085.ps
- Käufel, H. U., Renzini, A., & Stanghellini, L. 1993, *ApJ*, 410, 251
- King, I. R., et al. 1992, *ApJ*, 397, L35
- King, I. R., Stanford, S. A., & Crane, P. 1995, *AJ*, 109, 164
- Kurucz, R. L. 1992, in *IAU Symposium 149, The Stellar Populations of Galaxies*, ed. B. Barbuy & A. Renzini (Dordrecht: Kluwer Press), 225
- Lauer, T. R., et al. 1993, *AJ*, 106, 1436
- Lee, Y.-W. 1994, *ApJ*, 430, L113
- McClure, R. D., & Racine, R. 1969, *AJ*, 74, 1000
- McQuade, K., Calzetti, D., & Kinney, A. 1995, *ApJS*, 97, 331
- Meurer, G. R. 1995, in *Instrument Science Report FOC-083, The Photometric Accuracy of the FOC*, http://www.stsci.edu/ftp/instrument_news/FOC/Foc_isr/foc_isr083.ps
- Mitchell, K. J., Saffer, R. A., Howell, S. B., & Brown, T. M. 1998, *MNRAS*, in press
- Nota, A. et al. 1996, *FOC Instrument Handbook Version 7.0* (Baltimore: STScI)
- Osterbrock, D. E. 1989, in *Astrophysics of Gaseous Nebulae and Active Galactic Nuclei*, ed. A. Kelly (Mill Valley: University Science Books), 162
- Park, J.-H., & Lee, Y.-W. 1997, 476, 28
- Schneider, S. E., & Buckley, D. 1996, *ApJ*, 459, 606
- Tully, R. B. 1988, *Nearby Galaxies Catalogue* (Cambridge: University Press)
- Vassiliadis, E., & Wood, P. R. 1994, *ApJS*, 92, 125
- Worthey, G. 1994, *ApJS*, 95, 107
- Yi, S., Demarque, P., Oemler, Jr., A. 1997, *ApJ*, 486, 201

TABLE 1: *FOC* Observations and Photometry

	M 31		M 32	
R.A. ²⁰⁰⁰	0 ^h 42 ^m 44.74 ^s		0 ^h 42 ^m 41.53 ^s	
Dec. ²⁰⁰⁰	41°16'8.04''		40°51'51.82''	
<i>D</i> (kpc)	770		770	
<i>E</i> (<i>B</i> − <i>V</i>) ^a (mag)	0.11		0.11	
<i>m</i> ₁₅₅₀ − <i>V</i> ^b (mag)	3.51		4.50	
	F175W	F275W	F175W	F275W
EXPTIME (sec)	19773	8390	16179	8990
<i>m</i> _o ^c	19.43	21.47	19.43	21.47
PHOTFLAM ^d	6.12 × 10 ^{−17}	9.38 × 10 ^{−18}	6.12 × 10 ^{−17}	9.38 × 10 ^{−18}
Pivotal λ (Å)	1990	2800	1980	2800
Band width (Å)	386	323	386	323
PSF FWHM ^e (pixel)	4.6	4.0	4.3	3.9

^aFerguson & Davidsen (1993).^bBurstein et al. (1988).^cThe magnitude that produces 1 count/sec in the filter.^dThe flux (erg cm^{−2} s^{−1} Å^{−1}) that produces 1 count/sec in the filter.^eEstimated from PSF fitting in each image.

TABLE 2
M 31 SOURCE CATALOG

RA (J2000)	Dec (J2000)	m_{F175W} (mag)	error (mag)	m_{F275W} (mag)	error (mag)
0 ^h 42 ^m 44.041 ^s	41°16′02.71″	24.18	0.18	23.98	0.06
0 ^h 42 ^m 44.076 ^s	41°16′05.70″	22.29	0.07	22.60	0.03
0 ^h 42 ^m 44.081 ^s	41°16′04.91″	24.25	0.19	25.09	0.15
0 ^h 42 ^m 44.083 ^s	41°16′04.22″	22.09	0.04	22.57	0.03
0 ^h 42 ^m 44.087 ^s	41°16′03.50″	23.17:	0.07	23.72	0.05
0 ^h 42 ^m 44.091 ^s	41°16′06.97″	24.48	0.47	25.09	0.27
0 ^h 42 ^m 44.095 ^s	41°16′04.39″	24.48:	0.18	25.07	0.14
0 ^h 42 ^m 44.096 ^s	41°16′05.78″	24.08	0.18	24.97	0.14
0 ^h 42 ^m 44.098 ^s	41°16′06.30″	24.15	0.27	24.91	0.18
0 ^h 42 ^m 44.105 ^s	41°16′07.04″	24.35:	0.39	24.41	0.14
0 ^h 42 ^m 44.109 ^s	41°16′07.81″	24.02	0.35	25.44:	0.62
0 ^h 42 ^m 44.110 ^s	41°16′07.07″	24.39	0.38	25.49:	0.33
0 ^h 42 ^m 44.111 ^s	41°16′07.92″	24.04	0.36	25.26:	0.55
0 ^h 42 ^m 44.111 ^s	41°16′02.82″	23.99	0.12	24.34	0.07
0 ^h 42 ^m 44.112 ^s	41°16′08.33″	24.47:	0.55	24.18	0.24
0 ^h 42 ^m 44.117 ^s	41°16′06.84″	24.23	0.22	25.24	0.21
0 ^h 42 ^m 44.118 ^s	41°16′03.63″	24.28:	0.17	25.03	0.13
0 ^h 42 ^m 44.126 ^s	41°16′06.38″	24.30	0.18	24.67:	0.11
0 ^h 42 ^m 44.128 ^s	41°16′08.21″	23.73	0.29	25.23:	0.53
0 ^h 42 ^m 44.131 ^s	41°16′06.35″	24.07	0.14	24.31	0.09
0 ^h 42 ^m 44.132 ^s	41°16′08.17″	23.92	0.32	25.07:	0.38
0 ^h 42 ^m 44.142 ^s	41°16′07.98″	24.35:	0.38	25.06	0.29
0 ^h 42 ^m 44.142 ^s	41°16′05.45″	23.59	0.10	24.05	0.07
0 ^h 42 ^m 44.142 ^s	41°16′04.31″	23.97:	0.13	24.78	0.10
0 ^h 42 ^m 44.148 ^s	41°16′04.07″	24.46	0.18	24.60	0.09
0 ^h 42 ^m 44.149 ^s	41°16′07.63″	23.27	0.09	23.79:	0.07
0 ^h 42 ^m 44.149 ^s	41°16′07.70″	22.79	0.07	22.86	0.04
0 ^h 42 ^m 44.151 ^s	41°16′04.36″	23.22	0.08	23.37	0.04
0 ^h 42 ^m 44.153 ^s	41°16′07.62″	23.48	0.11	23.97	0.08
0 ^h 42 ^m 44.153 ^s	41°16′10.10″	24.36	0.43	25.40:	0.52
0 ^h 42 ^m 44.154 ^s	41°16′03.59″	22.10	0.04	22.52	0.03
0 ^h 42 ^m 44.154 ^s	41°16′06.49″	23.19	0.08	23.38	0.04
0 ^h 42 ^m 44.158 ^s	41°16′04.41″	23.72	0.10	24.67	0.09
0 ^h 42 ^m 44.171 ^s	41°16′06.76″	23.40	0.09	23.54	0.05
0 ^h 42 ^m 44.177 ^s	41°16′10.83″	22.67	0.08	22.91	0.04
0 ^h 42 ^m 44.181 ^s	41°16′07.13″	24.18:	0.16	24.76	0.14
0 ^h 42 ^m 44.181 ^s	41°16′11.23″	24.30	0.36	24.79	0.16
0 ^h 42 ^m 44.183 ^s	41°16′07.00″	24.23:	0.17	24.81	0.14
0 ^h 42 ^m 44.197 ^s	41°16′11.24″	24.33	0.28	25.44	0.22
0 ^h 42 ^m 44.202 ^s	41°16′11.90″	24.32	0.30	25.03	0.17
0 ^h 42 ^m 44.203 ^s	41°16′05.29″	24.50	0.17	24.86	0.11
0 ^h 42 ^m 44.204 ^s	41°16′06.38″	22.32	0.04	22.55	0.03
0 ^h 42 ^m 44.206 ^s	41°16′02.40″	24.00	0.12	24.40	0.08
0 ^h 42 ^m 44.206 ^s	41°16′12.74″	24.46:	0.39	24.64	0.13
0 ^h 42 ^m 44.210 ^s	41°16′12.73″	24.22	0.27	25.05:	0.17
0 ^h 42 ^m 44.215 ^s	41°16′05.77″	23.42	0.08	23.45	0.04
0 ^h 42 ^m 44.218 ^s	41°16′06.81″	24.01	0.13	24.39	0.09
0 ^h 42 ^m 44.222 ^s	41°16′07.21″	23.50	0.10	23.67	0.06
0 ^h 42 ^m 44.222 ^s	41°16′12.47″	24.37	0.21	24.15	0.07
0 ^h 42 ^m 44.223 ^s	41°16′07.38″	23.92	0.14	23.95	0.09
0 ^h 42 ^m 44.224 ^s	41°16′03.60″	24.24:	0.15	24.33	0.07
0 ^h 42 ^m 44.224 ^s	41°16′05.24″	24.34:	0.16	24.22	0.07
0 ^h 42 ^m 44.225 ^s	41°16′14.75″	23.07	0.12	23.54:	0.06
0 ^h 42 ^m 44.229 ^s	41°16′10.46″	23.39	0.10	23.33	0.05
0 ^h 42 ^m 44.230 ^s	41°16′06.68″	23.08	0.07	23.55	0.05
0 ^h 42 ^m 44.231 ^s	41°16′03.02″	24.38:	0.18	24.61	0.09

TABLE 2—*Continued*

RA (J2000)	Dec (J2000)	m_{F175W} (mag)	error (mag)	m_{F275W} (mag)	error (mag)
0 ^h 42 ^m 44.231 ^s	41°16′10.96″	24.31	0.17	24.71	0.11
0 ^h 42 ^m 44.231 ^s	41°16′03.27″	23.51	0.09	23.65	0.05
0 ^h 42 ^m 44.235 ^s	41°16′05.90″	24.43:	0.17	24.78	0.11
0 ^h 42 ^m 44.239 ^s	41°16′03.06″	22.64	0.05	23.16	0.04
0 ^h 42 ^m 44.240 ^s	41°16′03.31″	21.94	0.04	22.59	0.03
0 ^h 42 ^m 44.242 ^s	41°16′14.86″	24.25	0.30	24.71	0.17
0 ^h 42 ^m 44.242 ^s	41°16′03.42″	24.48	0.18	25.22:	0.13
0 ^h 42 ^m 44.244 ^s	41°16′03.35″	22.79:	0.06	23.93	0.06
0 ^h 42 ^m 44.244 ^s	41°16′13.79″	24.25	0.20	24.97	0.12
0 ^h 42 ^m 44.248 ^s	41°16′07.33″	23.82:	0.12	24.63	0.14
0 ^h 42 ^m 44.250 ^s	41°16′05.82″	23.91	0.12	24.19	0.07
0 ^h 42 ^m 44.258 ^s	41°16′04.74″	23.62	0.09	23.90	0.06
0 ^h 42 ^m 44.267 ^s	41°16′06.68″	22.06	0.04	22.23	0.02
0 ^h 42 ^m 44.267 ^s	41°16′11.72″	24.21:	0.14	24.04	0.06
0 ^h 42 ^m 44.273 ^s	41°16′06.94″	23.98	0.13	24.13	0.08
0 ^h 42 ^m 44.276 ^s	41°16′07.00″	24.34:	0.17	24.50	0.10
0 ^h 42 ^m 44.287 ^s	41°16′05.12″	23.77	0.11	24.39	0.08
0 ^h 42 ^m 44.294 ^s	41°16′06.76″	24.33	0.17	24.88	0.13
0 ^h 42 ^m 44.298 ^s	41°16′12.54″	23.64	0.10	23.24	0.04
0 ^h 42 ^m 44.302 ^s	41°16′10.82″	22.66	0.05	22.40	0.03
0 ^h 42 ^m 44.303 ^s	41°16′07.14″	24.21	0.15	24.95:	0.14
0 ^h 42 ^m 44.306 ^s	41°16′13.96″	24.45:	0.17	25.14	0.12
0 ^h 42 ^m 44.306 ^s	41°16′13.15″	24.42	0.16	25.11:	0.12
0 ^h 42 ^m 44.307 ^s	41°16′06.00″	21.37	0.03	21.65	0.02
0 ^h 42 ^m 44.310 ^s	41°16′12.11″	23.09	0.07	24.06	0.06
0 ^h 42 ^m 44.312 ^s	41°16′12.45″	24.21	0.14	24.55	0.09
0 ^h 42 ^m 44.313 ^s	41°16′10.55″	24.32	0.17	25.11	0.17
0 ^h 42 ^m 44.320 ^s	41°16′05.29″	22.01	0.04	22.07	0.02
0 ^h 42 ^m 44.321 ^s	41°16′06.01″	23.09	0.07	23.99	0.06
0 ^h 42 ^m 44.323 ^s	41°16′06.05″	23.13	0.07	23.73	0.05
0 ^h 42 ^m 44.324 ^s	41°16′06.75″	23.32	0.08	23.64	0.05
0 ^h 42 ^m 44.325 ^s	41°16′10.83″	23.95	0.12	24.71	0.11
0 ^h 42 ^m 44.327 ^s	41°16′04.59″	24.45:	0.17	24.50	0.09
0 ^h 42 ^m 44.327 ^s	41°16′10.54″	24.42	0.18	24.62	0.11
0 ^h 42 ^m 44.329 ^s	41°16′16.00″	23.75:	0.15	23.84	0.06
0 ^h 42 ^m 44.331 ^s	41°16′04.99″	24.37	0.17	25.39	0.17
0 ^h 42 ^m 44.331 ^s	41°16′04.14″	21.21	0.02	21.76	0.02
0 ^h 42 ^m 44.333 ^s	41°16′11.49″	23.47	0.08	24.12	0.07
0 ^h 42 ^m 44.334 ^s	41°16′05.15″	23.52	0.09	24.08	0.07
0 ^h 42 ^m 44.337 ^s	41°16′12.18″	23.74	0.10	24.53	0.09
0 ^h 42 ^m 44.344 ^s	41°16′07.70″	21.90	0.04	22.45	0.03
0 ^h 42 ^m 44.344 ^s	41°16′10.10″	23.43	0.09	24.22	0.10
0 ^h 42 ^m 44.352 ^s	41°16′06.09″	24.48	0.18	25.41	0.19
0 ^h 42 ^m 44.362 ^s	41°16′07.20″	24.50	0.19	24.87	0.13
0 ^h 42 ^m 44.364 ^s	41°16′06.37″	23.66	0.10	24.04	0.07
0 ^h 42 ^m 44.364 ^s	41°16′03.33″	23.69	0.10	24.16	0.06
0 ^h 42 ^m 44.365 ^s	41°16′05.38″	22.24	0.04	23.15	0.04
0 ^h 42 ^m 44.366 ^s	41°16′06.85″	23.50	0.09	23.70	0.06
0 ^h 42 ^m 44.367 ^s	41°16′06.24″	24.13	0.14	24.78	0.12
0 ^h 42 ^m 44.367 ^s	41°16′14.56″	24.06:	0.13	24.54	0.15
0 ^h 42 ^m 44.368 ^s	41°16′02.25″	23.54	0.09	24.07	0.06
0 ^h 42 ^m 44.369 ^s	41°16′14.74″	23.72	0.10	24.08	0.09
0 ^h 42 ^m 44.372 ^s	41°16′15.13″	24.35:	0.16	24.74	0.10
0 ^h 42 ^m 44.372 ^s	41°16′06.99″	23.66	0.10	23.90	0.06
0 ^h 42 ^m 44.373 ^s	41°16′10.12″	23.40	0.09	23.22	0.04
0 ^h 42 ^m 44.374 ^s	41°16′06.57″	23.30	0.08	23.39	0.05

TABLE 2—*Continued*

RA (J2000)	Dec (J2000)	m_{F175W} (mag)	error (mag)	m_{F275W} (mag)	error (mag)
$0^h42^m44.375^s$	$41^\circ16'09.80''$	24.48:	0.21	24.84	0.18
$0^h42^m44.377^s$	$41^\circ16'07.31''$	23.10	0.07	23.47	0.05
$0^h42^m44.378^s$	$41^\circ16'07.05''$	24.45:	0.18	24.48	0.09
$0^h42^m44.381^s$	$41^\circ16'11.46''$	24.48:	0.17	25.12	0.13
$0^h42^m44.383^s$	$41^\circ16'14.38''$	24.33:	0.16	24.31	0.13
$0^h42^m44.383^s$	$41^\circ16'14.78''$	22.19	0.04	22.21	0.02
$0^h42^m44.386^s$	$41^\circ16'12.00''$	24.01	0.12	24.55	0.09
$0^h42^m44.390^s$	$41^\circ16'04.75''$	24.40	0.17	25.10	0.14
$0^h42^m44.390^s$	$41^\circ16'10.33''$	24.23	0.15	23.95	0.07
$0^h42^m44.391^s$	$41^\circ16'08.12''$	24.18	0.15	25.03	0.16
$0^h42^m44.391^s$	$41^\circ16'09.12''$	23.52	0.10	24.25:	0.11
$0^h42^m44.392^s$	$41^\circ16'05.07''$	22.86	0.06	23.20	0.04
$0^h42^m44.393^s$	$41^\circ16'09.39''$	24.19	0.17	24.18	0.10
$0^h42^m44.393^s$	$41^\circ16'05.75''$	23.81	0.11	24.35:	0.08
$0^h42^m44.393^s$	$41^\circ16'05.71''$	23.77	0.11	24.01:	0.06
$0^h42^m44.394^s$	$41^\circ16'09.83''$	24.01	0.14	23.92	0.07
$0^h42^m44.394^s$	$41^\circ16'08.06''$	24.36	0.17	25.47:	0.22
$0^h42^m44.394^s$	$41^\circ16'07.29''$	24.45:	0.18	24.81	0.12
$0^h42^m44.394^s$	$41^\circ16'13.19''$	24.43:	0.19	25.37	0.28
$0^h42^m44.397^s$	$41^\circ16'05.62''$	23.54	0.09	24.16	0.07
$0^h42^m44.398^s$	$41^\circ16'06.39''$	23.84	0.12	24.14	0.07
$0^h42^m44.402^s$	$41^\circ16'05.54''$	23.74	0.11	24.36	0.08
$0^h42^m44.402^s$	$41^\circ16'11.60''$	23.65	0.10	23.33	0.04
$0^h42^m44.402^s$	$41^\circ16'09.14''$	21.30	0.03	21.62	0.02
$0^h42^m44.402^s$	$41^\circ16'06.13''$	24.06	0.14	24.21	0.08
$0^h42^m44.405^s$	$41^\circ16'05.66''$	24.49	0.19	25.49:	0.18
$0^h42^m44.415^s$	$41^\circ16'06.57''$	23.75	0.11	23.88	0.06
$0^h42^m44.416^s$	$41^\circ16'04.15''$	24.07:	0.13	24.60	0.09
$0^h42^m44.417^s$	$41^\circ16'09.91''$	24.16	0.15	24.67	0.12
$0^h42^m44.419^s$	$41^\circ16'12.04''$	24.02	0.12	24.80	0.10
$0^h42^m44.420^s$	$41^\circ16'05.16''$	24.46	0.18	24.98	0.13
$0^h42^m44.421^s$	$41^\circ16'05.78''$	23.82	0.12	24.77	0.12
$0^h42^m44.421^s$	$41^\circ16'04.17''$	23.40	0.08	24.52	0.08
$0^h42^m44.422^s$	$41^\circ16'05.73''$	24.10	0.14	24.78:	0.12
$0^h42^m44.422^s$	$41^\circ16'10.68''$	24.47	0.17	25.07	0.14
$0^h42^m44.423^s$	$41^\circ16'06.12''$	23.81	0.12	24.31	0.08
$0^h42^m44.423^s$	$41^\circ16'10.16''$	23.53	0.09	24.12	0.08
$0^h42^m44.434^s$	$41^\circ16'07.24''$	22.54	0.05	23.41	0.04
$0^h42^m44.434^s$	$41^\circ16'08.91''$	24.20	0.15	25.13	0.16
$0^h42^m44.434^s$	$41^\circ16'04.92''$	21.15	0.02	21.55	0.02
$0^h42^m44.435^s$	$41^\circ16'08.20''$	24.24	0.15	25.04	0.14
$0^h42^m44.435^s$	$41^\circ16'08.39''$	24.39	0.17	24.41	0.09
$0^h42^m44.440^s$	$41^\circ16'08.76''$	24.40:	0.17	24.73	0.11
$0^h42^m44.440^s$	$41^\circ16'10.09''$	23.44:	0.09	23.64	0.05
$0^h42^m44.442^s$	$41^\circ16'08.78''$	24.16:	0.14	24.71	0.11
$0^h42^m44.444^s$	$41^\circ16'02.67''$	24.13	0.13	24.96	0.11
$0^h42^m44.444^s$	$41^\circ16'09.82''$	23.29	0.08	23.69	0.06
$0^h42^m44.446^s$	$41^\circ16'06.67''$	24.20	0.16	25.07	0.15
$0^h42^m44.447^s$	$41^\circ16'07.35''$	23.97	0.13	24.89:	0.12
$0^h42^m44.447^s$	$41^\circ16'09.21''$	22.85	0.06	23.70	0.06
$0^h42^m44.447^s$	$41^\circ16'01.80''$	24.46	0.16	24.18	0.07
$0^h42^m44.448^s$	$41^\circ16'08.73''$	22.34	0.04	23.12	0.04
$0^h42^m44.448^s$	$41^\circ16'06.07''$	23.68	0.10	24.40	0.08
$0^h42^m44.450^s$	$41^\circ16'05.14''$	22.86	0.06	23.64	0.05
$0^h42^m44.451^s$	$41^\circ16'10.11''$	24.29	0.16	24.64	0.11
$0^h42^m44.452^s$	$41^\circ16'12.56''$	24.47:	0.16	25.12	0.12

TABLE 2—*Continued*

RA (J2000)	Dec (J2000)	m_{F175W} (mag)	error (mag)	m_{F275W} (mag)	error (mag)
0 ^h 42 ^m 44.452 ^s	41°16′08.54″	23.60	0.10	23.86	0.06
0 ^h 42 ^m 44.453 ^s	41°16′06.82″	24.34	0.17	25.25	0.17
0 ^h 42 ^m 44.454 ^s	41°16′06.02″	23.07	0.07	24.45	0.09
0 ^h 42 ^m 44.458 ^s	41°16′11.09″	23.39	0.08	24.40	0.08
0 ^h 42 ^m 44.459 ^s	41°16′09.15″	22.72	0.06	23.07	0.04
0 ^h 42 ^m 44.459 ^s	41°16′02.56″	24.13	0.13	24.54	0.08
0 ^h 42 ^m 44.462 ^s	41°16′15.73″	24.49:	0.33	25.39	0.14
0 ^h 42 ^m 44.463 ^s	41°16′09.61″	20.92	0.02	21.67	0.02
0 ^h 42 ^m 44.472 ^s	41°16′05.00″	24.18	0.14	25.26:	0.16
0 ^h 42 ^m 44.473 ^s	41°16′11.37″	23.55	0.09	23.83	0.05
0 ^h 42 ^m 44.474 ^s	41°16′09.63″	23.10	0.07	23.44	0.05
0 ^h 42 ^m 44.474 ^s	41°16′06.83″	23.75	0.11	24.45	0.09
0 ^h 42 ^m 44.476 ^s	41°16′06.18″	24.28	0.16	24.61	0.10
0 ^h 42 ^m 44.477 ^s	41°16′10.46″	24.08	0.13	24.24	0.07
0 ^h 42 ^m 44.477 ^s	41°16′05.04″	23.83	0.11	23.82	0.06
0 ^h 42 ^m 44.480 ^s	41°16′06.19″	24.36	0.17	24.85:	0.11
0 ^h 42 ^m 44.482 ^s	41°16′15.63″	23.49:	0.09	23.50	0.04
0 ^h 42 ^m 44.483 ^s	41°16′15.59″	23.93	0.12	24.00:	0.06
0 ^h 42 ^m 44.483 ^s	41°16′07.80″	23.80	0.11	24.03	0.07
0 ^h 42 ^m 44.485 ^s	41°16′03.50″	22.09	0.04	22.56	0.03
0 ^h 42 ^m 44.489 ^s	41°16′06.64″	23.07	0.07	23.57	0.05
0 ^h 42 ^m 44.498 ^s	41°16′10.42″	23.98	0.12	24.77	0.10
0 ^h 42 ^m 44.501 ^s	41°16′04.81″	22.94	0.06	23.94	0.06
0 ^h 42 ^m 44.501 ^s	41°16′10.20″	24.40	0.16	24.77	0.10
0 ^h 42 ^m 44.502 ^s	41°16′06.29″	24.33	0.16	24.12	0.07
0 ^h 42 ^m 44.503 ^s	41°16′01.57″	24.43:	0.17	25.16	0.14
0 ^h 42 ^m 44.503 ^s	41°16′06.79″	22.57	0.05	23.24	0.04
0 ^h 42 ^m 44.503 ^s	41°16′06.68″	24.02	0.13	25.00:	0.13
0 ^h 42 ^m 44.504 ^s	41°16′04.08″	24.49	0.17	25.44	0.16
0 ^h 42 ^m 44.505 ^s	41°16′10.90″	24.03	0.12	24.59	0.09
0 ^h 42 ^m 44.508 ^s	41°16′09.36″	24.19	0.15	24.21	0.07
0 ^h 42 ^m 44.509 ^s	41°16′12.87″	24.36:	0.15	24.15	0.06
0 ^h 42 ^m 44.512 ^s	41°16′10.59″	22.54	0.05	23.34	0.04
0 ^h 42 ^m 44.512 ^s	41°16′06.31″	23.25	0.08	24.21	0.07
0 ^h 42 ^m 44.513 ^s	41°16′15.17″	24.49:	0.16	25.09	0.12
0 ^h 42 ^m 44.516 ^s	41°16′08.36″	23.63	0.10	24.25	0.07
0 ^h 42 ^m 44.518 ^s	41°16′10.98″	23.68	0.10	25.24	0.14
0 ^h 42 ^m 44.521 ^s	41°16′04.72″	23.89	0.12	24.34	0.07
0 ^h 42 ^m 44.523 ^s	41°16′10.45″	23.92	0.12	24.17	0.07
0 ^h 42 ^m 44.523 ^s	41°16′08.97″	24.50	0.19	25.39	0.17
0 ^h 42 ^m 44.523 ^s	41°16′13.31″	24.40	0.15	25.46	0.15
0 ^h 42 ^m 44.530 ^s	41°16′03.52″	24.46:	0.17	25.29	0.14
0 ^h 42 ^m 44.531 ^s	41°16′03.50″	24.40:	0.16	25.30	0.14
0 ^h 42 ^m 44.532 ^s	41°16′11.66″	24.13	0.13	24.92	0.11
0 ^h 42 ^m 44.537 ^s	41°16′04.76″	23.54	0.09	24.29	0.07
0 ^h 42 ^m 44.540 ^s	41°16′07.34″	23.96	0.12	24.28	0.08
0 ^h 42 ^m 44.541 ^s	41°16′14.03″	23.14	0.07	24.45	0.07
0 ^h 42 ^m 44.543 ^s	41°16′06.95″	24.08:	0.14	24.36	0.08
0 ^h 42 ^m 44.544 ^s	41°16′15.09″	24.12:	0.12	24.49	0.08
0 ^h 42 ^m 44.545 ^s	41°16′06.47″	24.38	0.17	24.98:	0.12
0 ^h 42 ^m 44.549 ^s	41°16′06.47″	24.17:	0.15	24.40	0.08
0 ^h 42 ^m 44.550 ^s	41°16′01.48″	23.70	0.10	23.33	0.04
0 ^h 42 ^m 44.556 ^s	41°16′09.15″	23.91	0.12	24.86	0.11
0 ^h 42 ^m 44.557 ^s	41°16′12.21″	24.20	0.14	24.81	0.10
0 ^h 42 ^m 44.561 ^s	41°16′12.46″	23.97	0.12	24.49	0.08
0 ^h 42 ^m 44.563 ^s	41°16′12.82″	22.11	0.04	22.54	0.03

TABLE 2—*Continued*

RA (J2000)	Dec (J2000)	m_{F175W} (mag)	error (mag)	m_{F275W} (mag)	error (mag)
0 ^h 42 ^m 44.565 ^s	41°16′06.05″	23.97	0.12	24.95	0.12
0 ^h 42 ^m 44.566 ^s	41°16′10.30″	24.00	0.12	24.32	0.07
0 ^h 42 ^m 44.571 ^s	41°16′06.33″	24.32	0.16	25.00	0.12
0 ^h 42 ^m 44.576 ^s	41°16′07.53″	23.69	0.10	24.92	0.12
0 ^h 42 ^m 44.577 ^s	41°16′03.16″	23.81	0.11	24.10	0.06
0 ^h 42 ^m 44.581 ^s	41°16′12.52″	24.39	0.15	24.29	0.07
0 ^h 42 ^m 44.582 ^s	41°16′07.87″	24.32	0.16	24.86:	0.12
0 ^h 42 ^m 44.582 ^s	41°16′04.89″	23.83	0.11	24.15	0.07
0 ^h 42 ^m 44.585 ^s	41°16′07.94″	24.39	0.17	24.49	0.09
0 ^h 42 ^m 44.585 ^s	41°16′14.82″	24.34	0.15	24.86	0.10
0 ^h 42 ^m 44.589 ^s	41°16′04.43″	24.32:	0.16	24.78	0.10
0 ^h 42 ^m 44.593 ^s	41°16′05.84″	24.08	0.13	24.61	0.09
0 ^h 42 ^m 44.594 ^s	41°16′15.40″	23.72	0.10	23.98	0.06
0 ^h 42 ^m 44.595 ^s	41°16′11.64″	23.75	0.10	24.39	0.07
0 ^h 42 ^m 44.596 ^s	41°16′08.02″	24.35	0.16	25.08:	0.13
0 ^h 42 ^m 44.600 ^s	41°16′12.56″	23.44	0.08	23.58	0.05
0 ^h 42 ^m 44.603 ^s	41°16′08.06″	22.03	0.04	22.43	0.03
0 ^h 42 ^m 44.604 ^s	41°16′08.51″	23.40	0.08	23.90	0.06
0 ^h 42 ^m 44.608 ^s	41°16′07.21″	24.11	0.14	25.29	0.16
0 ^h 42 ^m 44.610 ^s	41°16′12.40″	23.88	0.11	23.95	0.06
0 ^h 42 ^m 44.611 ^s	41°16′10.56″	22.00	0.04	22.80	0.03
0 ^h 42 ^m 44.613 ^s	41°16′13.73″	24.24:	0.14	25.01	0.11
0 ^h 42 ^m 44.613 ^s	41°16′12.94″	24.11	0.12	24.54	0.08
0 ^h 42 ^m 44.615 ^s	41°16′10.46″	24.45:	0.16	25.22	0.14
0 ^h 42 ^m 44.617 ^s	41°16′13.62″	22.79	0.06	23.62	0.05
0 ^h 42 ^m 44.618 ^s	41°16′07.63″	24.05	0.14	25.40	0.17
0 ^h 42 ^m 44.619 ^s	41°16′07.13″	24.25:	0.15	24.86	0.11
0 ^h 42 ^m 44.619 ^s	41°16′14.60″	21.06 ^a	0.02	21.26 ^a	0.01
0 ^h 42 ^m 44.619 ^s	41°16′09.69″	24.45:	0.17	25.10	0.13
0 ^h 42 ^m 44.620 ^s	41°16′12.83″	24.47	0.16	23.41	0.04
0 ^h 42 ^m 44.626 ^s	41°16′12.28″	24.34	0.15	25.26	0.14
0 ^h 42 ^m 44.632 ^s	41°16′12.88″	24.19	0.13	24.78	0.10
0 ^h 42 ^m 44.633 ^s	41°16′09.52″	23.91	0.12	24.16	0.07
0 ^h 42 ^m 44.635 ^s	41°16′07.20″	24.34	0.17	24.67	0.10
0 ^h 42 ^m 44.636 ^s	41°16′12.19″	24.25	0.14	24.68	0.09
0 ^h 42 ^m 44.636 ^s	41°16′10.21″	24.42:	0.17	25.00	0.12
0 ^h 42 ^m 44.637 ^s	41°16′10.92″	24.26:	0.14	24.86	0.10
0 ^h 42 ^m 44.639 ^s	41°16′07.24″	24.43	0.18	25.47:	0.18
0 ^h 42 ^m 44.639 ^s	41°16′14.88″	23.92	0.11	24.51	0.08
0 ^h 42 ^m 44.639 ^s	41°16′13.72″	24.13	0.13	25.22:	0.13
0 ^h 42 ^m 44.640 ^s	41°16′11.03″	24.29	0.14	24.30	0.07
0 ^h 42 ^m 44.647 ^s	41°16′08.80″	24.49:	0.18	24.77	0.10
0 ^h 42 ^m 44.651 ^s	41°16′08.99″	23.66	0.10	23.93	0.06
0 ^h 42 ^m 44.653 ^s	41°16′08.88″	24.46:	0.17	25.10	0.13
0 ^h 42 ^m 44.659 ^s	41°16′08.65″	23.73	0.11	24.16	0.07
0 ^h 42 ^m 44.662 ^s	41°16′07.03″	24.03	0.13	25.13	0.14
0 ^h 42 ^m 44.664 ^s	41°16′03.57″	24.32	0.16	25.39	0.15
0 ^h 42 ^m 44.664 ^s	41°16′06.22″	24.01	0.13	23.69	0.05
0 ^h 42 ^m 44.664 ^s	41°16′02.70″	23.66	0.10	24.28	0.07
0 ^h 42 ^m 44.665 ^s	41°16′14.74″	24.01	0.12	24.35	0.07
0 ^h 42 ^m 44.669 ^s	41°16′09.27″	24.32	0.16	25.28	0.16
0 ^h 42 ^m 44.669 ^s	41°16′01.08″	24.16	0.14	23.66	0.08
0 ^h 42 ^m 44.674 ^s	41°16′06.87″	23.97	0.13	24.20	0.07
0 ^h 42 ^m 44.674 ^s	41°16′07.16″	24.36	0.17	24.93	0.12
0 ^h 42 ^m 44.677 ^s	41°16′02.63″	24.10	0.13	24.37	0.07
0 ^h 42 ^m 44.679 ^s	41°16′02.62″	24.22:	0.14	24.62	0.09

TABLE 2—*Continued*

RA (J2000)	Dec (J2000)	m_{F175W} (mag)	error (mag)	m_{F275W} (mag)	error (mag)
0 ^h 42 ^m 44.682 ^s	41°16′06.27″	23.76:	0.11	24.62	0.09
0 ^h 42 ^m 44.682 ^s	41°16′13.52″	23.94	0.11	24.56	0.08
0 ^h 42 ^m 44.684 ^s	41°16′04.89″	24.22	0.15	24.78	0.10
0 ^h 42 ^m 44.685 ^s	41°16′04.28″	24.45	0.17	25.34	0.15
0 ^h 42 ^m 44.685 ^s	41°16′06.28″	23.12	0.07	23.98:	0.06
0 ^h 42 ^m 44.691 ^s	41°16′06.23″	21.53	0.03	22.04	0.02
0 ^h 42 ^m 44.692 ^s	41°16′07.44″	23.67	0.10	23.77	0.06
0 ^h 42 ^m 44.693 ^s	41°16′04.25″	22.11	0.04	22.83	0.03
0 ^h 42 ^m 44.693 ^s	41°16′05.80″	24.49:	0.19	25.07	0.13
0 ^h 42 ^m 44.696 ^s	41°16′14.38″	24.10:	0.12	24.07	0.06
0 ^h 42 ^m 44.698 ^s	41°16′07.02″	24.38	0.18	24.86	0.11
0 ^h 42 ^m 44.699 ^s	41°16′03.05″	23.97	0.12	24.40	0.07
0 ^h 42 ^m 44.702 ^s	41°16′04.70″	24.16:	0.14	24.34	0.08
0 ^h 42 ^m 44.702 ^s	41°16′14.45″	21.35 ^b	0.03	21.28 ^b	0.01
0 ^h 42 ^m 44.703 ^s	41°16′04.49″	24.36	0.17	24.58	0.09
0 ^h 42 ^m 44.710 ^s	41°16′06.55″	23.42	0.09	24.26	0.07
0 ^h 42 ^m 44.711 ^s	41°16′04.82″	24.27:	0.15	24.12	0.06
0 ^h 42 ^m 44.712 ^s	41°16′08.42″	23.40	0.08	23.93	0.06
0 ^h 42 ^m 44.713 ^s	41°16′05.57″	24.35:	0.16	25.05	0.12
0 ^h 42 ^m 44.715 ^s	41°16′05.46″	22.73	0.06	23.56	0.05
0 ^h 42 ^m 44.721 ^s	41°16′11.84″	24.47:	0.16	25.23	0.13
0 ^h 42 ^m 44.721 ^s	41°16′11.32″	24.33	0.15	24.58	0.09
0 ^h 42 ^m 44.723 ^s	41°16′08.59″	24.46	0.18	24.51	0.09
0 ^h 42 ^m 44.725 ^s	41°16′04.94″	23.46	0.09	23.10	0.04
0 ^h 42 ^m 44.728 ^s	41°16′01.74″	23.89	0.12	24.08	0.06
0 ^h 42 ^m 44.731 ^s	41°16′12.54″	22.31	0.04	22.94	0.03
0 ^h 42 ^m 44.732 ^s	41°16′03.61″	23.56	0.09	24.12	0.06
0 ^h 42 ^m 44.734 ^s	41°16′03.58″	23.71:	0.10	24.03	0.06
0 ^h 42 ^m 44.739 ^s	41°16′01.31″	22.42	0.04	22.26	0.02
0 ^h 42 ^m 44.740 ^s	41°16′14.12″	23.95	0.11	24.33	0.07
0 ^h 42 ^m 44.741 ^s	41°16′03.95″	24.23	0.14	25.23	0.14
0 ^h 42 ^m 44.742 ^s	41°16′03.94″	24.30:	0.15	25.28	0.14
0 ^h 42 ^m 44.744 ^s	41°16′09.93″	24.11:	0.13	24.69	0.09
0 ^h 42 ^m 44.744 ^s	41°16′02.10″	24.42:	0.17	25.49	0.16
0 ^h 42 ^m 44.744 ^s	41°16′12.28″	23.19	0.07	24.00	0.06
0 ^h 42 ^m 44.745 ^s	41°16′09.90″	23.72	0.10	24.46	0.08
0 ^h 42 ^m 44.745 ^s	41°16′13.11″	24.35	0.15	24.79	0.09
0 ^h 42 ^m 44.745 ^s	41°16′11.31″	22.65	0.05	22.40	0.03
0 ^h 42 ^m 44.748 ^s	41°16′11.38″	23.88:	0.11	24.20	0.07
0 ^h 42 ^m 44.749 ^s	41°16′08.57″	24.02	0.13	25.11	0.13
0 ^h 42 ^m 44.749 ^s	41°16′08.77″	24.02	0.13	25.42	0.17
0 ^h 42 ^m 44.758 ^s	41°16′01.95″	23.38	0.09	24.57	0.13
0 ^h 42 ^m 44.758 ^s	41°16′14.90″	23.83	0.11	24.44	0.07
0 ^h 42 ^m 44.760 ^s	41°16′12.88″	23.47	0.08	24.06	0.06
0 ^h 42 ^m 44.767 ^s	41°16′09.14″	23.91	0.12	24.59	0.09
0 ^h 42 ^m 44.771 ^s	41°16′04.66″	24.27	0.15	25.18	0.13
0 ^h 42 ^m 44.773 ^s	41°16′04.35″	23.56	0.09	24.18	0.07
0 ^h 42 ^m 44.774 ^s	41°16′09.20″	21.90	0.04	22.56	0.03
0 ^h 42 ^m 44.776 ^s	41°16′10.54″	23.78	0.10	24.00	0.06
0 ^h 42 ^m 44.778 ^s	41°16′05.55″	23.68	0.10	24.14	0.06
0 ^h 42 ^m 44.782 ^s	41°16′07.95″	22.43	0.05	23.35	0.04
0 ^h 42 ^m 44.786 ^s	41°16′04.80″	23.98	0.12	24.01	0.06
0 ^h 42 ^m 44.791 ^s	41°16′03.31″	23.48	0.08	23.64	0.05
0 ^h 42 ^m 44.800 ^s	41°16′08.63″	24.18	0.14	24.69	0.09
0 ^h 42 ^m 44.802 ^s	41°16′12.62″	24.31	0.15	25.47	0.15
0 ^h 42 ^m 44.806 ^s	41°16′14.69″	24.00	0.12	24.31	0.07

TABLE 2—*Continued*

RA (J2000)	Dec (J2000)	m_{F175W} (mag)	error (mag)	m_{F275W} (mag)	error (mag)
0 ^h 42 ^m 44.814 ^s	41°16′07.71″	24.16	0.14	24.73	0.10
0 ^h 42 ^m 44.820 ^s	41°16′09.58″	23.69:	0.10	24.54	0.09
0 ^h 42 ^m 44.821 ^s	41°16′13.38″	22.76	0.05	23.28	0.04
0 ^h 42 ^m 44.821 ^s	41°16′09.49″	21.39	0.03	21.95	0.02
0 ^h 42 ^m 44.833 ^s	41°16′09.61″	24.49:	0.18	24.95	0.11
0 ^h 42 ^m 44.835 ^s	41°16′02.55″	24.26	0.14	24.30	0.07
0 ^h 42 ^m 44.837 ^s	41°16′10.69″	23.54	0.09	23.59	0.05
0 ^h 42 ^m 44.837 ^s	41°16′10.29″	24.47:	0.18	25.03	0.12
0 ^h 42 ^m 44.837 ^s	41°16′09.67″	22.88	0.06	23.68	0.05
0 ^h 42 ^m 44.839 ^s	41°16′05.09″	23.82	0.11	24.15	0.07
0 ^h 42 ^m 44.846 ^s	41°16′10.90″	22.13	0.04	22.80	0.03
0 ^h 42 ^m 44.849 ^s	41°16′12.59″	23.17	0.07	24.20	0.07
0 ^h 42 ^m 44.851 ^s	41°16′12.28″	22.90	0.06	22.73	0.03
0 ^h 42 ^m 44.853 ^s	41°16′03.83″	24.03	0.12	24.48	0.08
0 ^h 42 ^m 44.860 ^s	41°16′14.55″	24.15	0.13	24.53	0.08
0 ^h 42 ^m 44.863 ^s	41°16′11.48″	24.32:	0.15	25.14	0.12
0 ^h 42 ^m 44.864 ^s	41°16′07.17″	23.88	0.11	24.45	0.08
0 ^h 42 ^m 44.867 ^s	41°16′10.52″	24.17	0.14	24.76	0.10
0 ^h 42 ^m 44.870 ^s	41°16′06.41″	24.46:	0.17	25.50	0.16
0 ^h 42 ^m 44.872 ^s	41°16′11.38″	24.44	0.17	25.11	0.12
0 ^h 42 ^m 44.875 ^s	41°16′09.07″	23.91	0.12	25.07:	0.12
0 ^h 42 ^m 44.875 ^s	41°16′12.34″	23.99	0.12	24.33	0.07
0 ^h 42 ^m 44.879 ^s	41°16′09.05″	23.94	0.12	24.38	0.08
0 ^h 42 ^m 44.883 ^s	41°16′09.07″	24.45	0.18	25.13	0.13
0 ^h 42 ^m 44.884 ^s	41°16′09.46″	23.98	0.13	24.79	0.10
0 ^h 42 ^m 44.888 ^s	41°16′03.20″	23.33	0.08	23.55	0.04
0 ^h 42 ^m 44.889 ^s	41°16′12.68″	23.65	0.09	24.09	0.06
0 ^h 42 ^m 44.890 ^s	41°16′11.06″	23.84	0.11	24.09	0.06
0 ^h 42 ^m 44.891 ^s	41°16′02.51″	22.00	0.04	22.12	0.02
0 ^h 42 ^m 44.894 ^s	41°16′03.92″	23.82	0.10	24.21	0.07
0 ^h 42 ^m 44.897 ^s	41°16′01.64″	24.32	0.16	24.53	0.11
0 ^h 42 ^m 44.900 ^s	41°16′09.55″	23.86	0.12	24.37	0.08
0 ^h 42 ^m 44.915 ^s	41°16′04.31″	23.93:	0.11	24.82	0.10
0 ^h 42 ^m 44.917 ^s	41°16′10.79″	23.85	0.11	24.39	0.08
0 ^h 42 ^m 44.922 ^s	41°16′04.30″	22.19	0.04	22.77	0.03
0 ^h 42 ^m 44.925 ^s	41°16′14.74″	23.67	0.13	24.22	0.07
0 ^h 42 ^m 44.926 ^s	41°16′06.11″	24.30:	0.15	24.58	0.08
0 ^h 42 ^m 44.932 ^s	41°16′13.58″	23.84	0.10	24.03	0.06
0 ^h 42 ^m 44.953 ^s	41°16′12.66″	24.19	0.14	24.38	0.07
0 ^h 42 ^m 44.959 ^s	41°16′11.61″	23.03	0.06	22.78	0.03
0 ^h 42 ^m 44.972 ^s	41°16′09.24″	22.27	0.04	23.17	0.04
0 ^h 42 ^m 44.977 ^s	41°16′07.74″	24.47	0.17	24.71	0.09
0 ^h 42 ^m 44.977 ^s	41°16′13.96″	23.60:	0.09	24.12	0.06
0 ^h 42 ^m 44.978 ^s	41°16′12.45″	22.81	0.06	23.13	0.04
0 ^h 42 ^m 44.979 ^s	41°16′12.86″	24.38	0.16	24.86	0.10
0 ^h 42 ^m 45.000 ^s	41°16′01.02″	24.30	0.14	25.14:	0.12
0 ^h 42 ^m 45.001 ^s	41°16′07.25″	24.23:	0.14	24.16	0.06
0 ^h 42 ^m 45.001 ^s	41°16′01.07″	24.30:	0.14	24.59	0.08
0 ^h 42 ^m 45.009 ^s	41°16′02.28″	23.83	0.10	24.03	0.06
0 ^h 42 ^m 45.009 ^s	41°16′09.57″	24.44:	0.17	25.39	0.14
0 ^h 42 ^m 45.017 ^s	41°16′10.59″	23.22	0.07	24.07	0.06
0 ^h 42 ^m 45.018 ^s	41°16′07.97″	23.27	0.07	23.32	0.04
0 ^h 42 ^m 45.022 ^s	41°16′11.56″	24.18:	0.14	24.49	0.08
0 ^h 42 ^m 45.023 ^s	41°16′02.60″	24.28	0.14	25.04	0.11
0 ^h 42 ^m 45.024 ^s	41°16′10.54″	23.76	0.10	24.16	0.06
0 ^h 42 ^m 45.024 ^s	41°16′08.42″	24.13	0.13	24.19	0.07

TABLE 2—*Continued*

RA (J2000)	Dec (J2000)	m_{F175W} (mag)	error (mag)	m_{F275W} (mag)	error (mag)
0 ^h 42 ^m 45.036 ^s	41°16′10.94″	24.26:	0.15	25.26	0.13
0 ^h 42 ^m 45.038 ^s	41°16′13.38″	23.85	0.11	23.94	0.06
0 ^h 42 ^m 45.048 ^s	41°16′09.67″	24.04	0.12	24.26	0.07
0 ^h 42 ^m 45.052 ^s	41°16′13.41″	24.48	0.17	24.49	0.08
0 ^h 42 ^m 45.054 ^s	41°16′01.50″	23.76	0.10	24.86	0.10
0 ^h 42 ^m 45.056 ^s	41°16′10.56″	23.71	0.10	24.41	0.07
0 ^h 42 ^m 45.059 ^s	41°16′13.10″	22.17	0.04	22.86	0.03
0 ^h 42 ^m 45.071 ^s	41°16′10.05″	24.33:	0.15	24.85	0.10
0 ^h 42 ^m 45.084 ^s	41°16′13.52″	24.42	0.17	24.61:	0.09
0 ^h 42 ^m 45.085 ^s	41°16′12.16″	24.09:	0.12	24.55	0.08
0 ^h 42 ^m 45.086 ^s	41°16′09.75″	23.86:	0.11	24.96	0.11
0 ^h 42 ^m 45.112 ^s	41°16′09.02″	22.75	0.05	22.81	0.03
0 ^h 42 ^m 45.117 ^s	41°16′06.89″	24.18:	0.14	24.90	0.10
0 ^h 42 ^m 45.135 ^s	41°16′05.95″	24.38:	0.15	25.09	0.11
0 ^h 42 ^m 45.136 ^s	41°16′08.82″	23.93	0.12	24.43	0.08
0 ^h 42 ^m 45.136 ^s	41°16′07.39″	23.14	0.07	23.45	0.04
0 ^h 42 ^m 45.144 ^s	41°16′05.89″	22.82	0.06	23.26	0.04
0 ^h 42 ^m 45.152 ^s	41°16′04.34″	24.02	0.12	24.18	0.06
0 ^h 42 ^m 45.157 ^s	41°16′07.95″	23.86	0.11	23.83	0.05
0 ^h 42 ^m 45.185 ^s	41°16′04.00″	24.40:	0.16	24.11	0.06
0 ^h 42 ^m 45.188 ^s	41°16′02.74″	24.17	0.14	25.22:	0.17
0 ^h 42 ^m 45.194 ^s	41°16′12.98″	24.43:	0.17	25.20	0.12
0 ^h 42 ^m 45.195 ^s	41°16′12.22″	24.28:	0.15	24.11	0.06
0 ^h 42 ^m 45.209 ^s	41°16′07.15″	22.69	0.05	22.16	0.02
0 ^h 42 ^m 45.219 ^s	41°16′05.87″	23.80	0.11	24.16	0.06
0 ^h 42 ^m 45.230 ^s	41°16′10.91″	24.21:	0.14	24.33	0.07
0 ^h 42 ^m 45.232 ^s	41°16′11.33″	23.69	0.10	24.23	0.07
0 ^h 42 ^m 45.233 ^s	41°16′06.10″	23.96:	0.12	24.59	0.08
0 ^h 42 ^m 45.234 ^s	41°16′10.93″	24.40	0.16	25.13:	0.12
0 ^h 42 ^m 45.236 ^s	41°16′06.07″	23.93:	0.12	24.59	0.08
0 ^h 42 ^m 45.238 ^s	41°16′06.02″	24.26	0.15	25.28:	0.13
0 ^h 42 ^m 45.251 ^s	41°16′11.51″	24.23	0.14	25.31	0.14
0 ^h 42 ^m 45.252 ^s	41°16′11.46″	24.36:	0.15	24.99	0.11
0 ^h 42 ^m 45.270 ^s	41°16′13.64″	23.28:	0.08	23.84	0.05
0 ^h 42 ^m 45.284 ^s	41°16′09.38″	21.46	0.03	21.91	0.02
0 ^h 42 ^m 45.291 ^s	41°16′11.79″	23.80:	0.10	24.30	0.07
0 ^h 42 ^m 45.292 ^s	41°16′13.45″	24.49:	0.18	24.66	0.09
0 ^h 42 ^m 45.314 ^s	41°16′11.01″	24.32	0.15	24.48	0.08
0 ^h 42 ^m 45.334 ^s	41°16′10.32″	24.41:	0.16	24.66	0.09
0 ^h 42 ^m 45.365 ^s	41°16′13.78″	23.94	0.19	24.39	0.08
0 ^h 42 ^m 45.420 ^s	41°16′13.36″	24.34	0.20	25.41:	0.33

^{a,b}These stars have photometric problems and are discussed in §2 and §3.2.

TABLE 3
M 32 SOURCE CATALOG

RA (J2000)	Dec (J2000)	m_{F175W} (mag)	error (mag)	m_{F275W} (mag)	error (mag)
0 ^h 42 ^m 40.804 ^s	40°51'46.37''	24.22:	0.27	24.38	0.12
0 ^h 42 ^m 40.805 ^s	40°51'46.42''	24.09	0.24	24.46:	0.13
0 ^h 42 ^m 40.812 ^s	40°51'46.39''	23.53	0.15	24.43:	0.13
0 ^h 42 ^m 40.823 ^s	40°51'46.33''	23.92	0.19	24.90:	0.19
0 ^h 42 ^m 40.870 ^s	40°51'49.92''	24.19:	0.33	25.05	0.19
0 ^h 42 ^m 40.910 ^s	40°51'51.66''	23.56:	0.20	24.54	0.13
0 ^h 42 ^m 40.915 ^s	40°51'52.12''	23.91:	0.27	25.45	0.29
0 ^h 42 ^m 40.918 ^s	40°51'52.02''	23.68:	0.23	24.55	0.13
0 ^h 42 ^m 40.922 ^s	40°51'52.25''	23.72:	0.23	25.17	0.22
0 ^h 42 ^m 40.936 ^s	40°51'49.03''	24.39	0.17	24.28	0.06
0 ^h 42 ^m 40.964 ^s	40°51'54.34''	24.15:	0.33	25.34	0.26
0 ^h 42 ^m 40.968 ^s	40°51'55.01''	24.01	0.30	24.86	0.19
0 ^h 42 ^m 40.969 ^s	40°51'55.05''	24.09:	0.32	25.02	0.22
0 ^h 42 ^m 40.977 ^s	40°51'55.42''	24.38:	0.40	25.28	0.28
0 ^h 42 ^m 40.980 ^s	40°51'48.49''	24.18:	0.14	24.77	0.08
0 ^h 42 ^m 40.987 ^s	40°51'55.65''	24.01:	0.29	25.02	0.21
0 ^h 42 ^m 41.005 ^s	40°51'55.28''	24.15	0.19	24.83	0.10
0 ^h 42 ^m 41.010 ^s	40°51'51.52''	23.95	0.12	24.83	0.09
0 ^h 42 ^m 41.011 ^s	40°51'47.91''	24.32	0.16	25.12	0.10
0 ^h 42 ^m 41.016 ^s	40°51'46.03''	24.10	0.17	24.18	0.06
0 ^h 42 ^m 41.030 ^s	40°51'50.67''	24.43	0.17	25.31:	0.12
0 ^h 42 ^m 41.033 ^s	40°51'53.85''	24.48	0.18	24.83	0.09
0 ^h 42 ^m 41.040 ^s	40°51'51.84''	22.25	0.04	22.05	0.02
0 ^h 42 ^m 41.064 ^s	40°51'52.97''	23.84	0.11	24.31	0.07
0 ^h 42 ^m 41.137 ^s	40°51'59.71''	23.20	0.08	23.96	0.06
0 ^h 42 ^m 41.144 ^s	40°51'56.50''	23.95:	0.12	24.12	0.06
0 ^h 42 ^m 41.167 ^s	40°51'58.81''	24.39:	0.16	24.91	0.10
0 ^h 42 ^m 41.188 ^s	40°51'50.80''	23.37	0.09	24.06	0.06
0 ^h 42 ^m 41.226 ^s	40°51'45.51''	24.15	0.17	24.25	0.06
0 ^h 42 ^m 41.243 ^s	40°51'58.49''	23.45	0.09	23.82	0.05
0 ^h 42 ^m 41.274 ^s	40°51'53.95''	24.27	0.16	24.46	0.08
0 ^h 42 ^m 41.276 ^s	40°51'56.87''	24.47	0.17	25.48:	0.16
0 ^h 42 ^m 41.282 ^s	40°51'54.57''	24.30	0.16	25.18	0.13
0 ^h 42 ^m 41.309 ^s	40°51'54.24''	24.06	0.14	25.32	0.15
0 ^h 42 ^m 41.312 ^s	40°51'57.01''	24.04	0.13	24.34	0.07
0 ^h 42 ^m 41.318 ^s	40°51'45.45''	23.45:	0.10	24.49	0.12
0 ^h 42 ^m 41.326 ^s	40°51'47.21''	23.10	0.07	23.68	0.05
0 ^h 42 ^m 41.342 ^s	40°51'51.38''	24.15	0.15	24.59	0.09
0 ^h 42 ^m 41.363 ^s	40°51'57.11''	22.93	0.06	23.61	0.05
0 ^h 42 ^m 41.364 ^s	40°51'58.59''	23.77	0.11	24.60	0.09
0 ^h 42 ^m 41.370 ^s	40°51'57.66''	24.47:	0.18	24.93	0.11
0 ^h 42 ^m 41.373 ^s	40°51'53.86''	22.16	0.04	22.53	0.03
0 ^h 42 ^m 41.380 ^s	40°51'53.91''	24.42:	0.18	25.26	0.16
0 ^h 42 ^m 41.380 ^s	40°51'53.20''	21.47	0.03	21.87	0.02
0 ^h 42 ^m 41.383 ^s	40°51'49.25''	23.94	0.13	24.34	0.07
0 ^h 42 ^m 41.384 ^s	40°51'44.98''	24.04	0.18	25.49	0.15
0 ^h 42 ^m 41.407 ^s	40°51'48.04''	21.96	0.04	22.49	0.03
0 ^h 42 ^m 41.413 ^s	40°51'55.90''	23.69	0.11	24.58	0.10
0 ^h 42 ^m 41.420 ^s	40°51'52.29''	23.73	0.12	24.61	0.11
0 ^h 42 ^m 41.428 ^s	40°51'57.24''	24.00	0.13	24.57	0.09
0 ^h 42 ^m 41.441 ^s	40°51'57.38''	24.08	0.14	24.48	0.08
0 ^h 42 ^m 41.449 ^s	40°51'57.49''	24.37:	0.17	24.99	0.12
0 ^h 42 ^m 41.458 ^s	40°51'57.35''	23.92	0.12	24.11	0.07
0 ^h 42 ^m 41.460 ^s	40°51'51.50''	24.33	0.19	25.11	0.16
0 ^h 42 ^m 41.469 ^s	40°51'52.30''	24.29	0.18	24.31	0.09
0 ^h 42 ^m 41.470 ^s	40°51'45.95''	24.29	0.18	25.26	0.13

TABLE 3—*Continued*

RA (J2000)	Dec (J2000)	m_{F175W} (mag)	error (mag)	m_{F275W} (mag)	error (mag)
0 ^h 42 ^m 41.472 ^s	40°51'51.31''	24.38:	0.20	25.02	0.15
0 ^h 42 ^m 41.481 ^s	40°51'49.70''	24.13	0.15	24.71	0.10
0 ^h 42 ^m 41.482 ^s	40°51'54.36''	24.02	0.14	24.43	0.11
0 ^h 42 ^m 41.494 ^s	40°51'56.11''	24.23	0.16	24.60	0.13
0 ^h 42 ^m 41.497 ^s	40°51'55.83''	23.58	0.11	23.76	0.07
0 ^h 42 ^m 41.497 ^s	40°51'49.40''	24.34	0.17	25.19	0.15
0 ^h 42 ^m 41.506 ^s	40°51'55.30''	23.91	0.14	24.47	0.13
0 ^h 42 ^m 41.510 ^s	40°51'48.88''	24.11	0.14	24.82	0.11
0 ^h 42 ^m 41.513 ^s	40°51'57.61''	24.45:	0.17	25.15	0.15
0 ^h 42 ^m 41.526 ^s	40°51'51.77''	22.33	0.05	23.31	0.05
0 ^h 42 ^m 41.549 ^s	40°51'58.93''	24.10:	0.14	24.61	0.09
0 ^h 42 ^m 41.552 ^s	40°51'54.30''	23.85	0.16	24.12	0.16
0 ^h 42 ^m 41.568 ^s	40°51'56.70''	23.68	0.11	24.22	0.10
0 ^h 42 ^m 41.573 ^s	40°51'50.55''	22.59	0.06	23.43	0.05
0 ^h 42 ^m 41.577 ^s	40°51'56.34''	24.03	0.15	24.20	0.12
0 ^h 42 ^m 41.577 ^s	40°51'56.89''	24.50	0.20	25.43:	0.26
0 ^h 42 ^m 41.582 ^s	40°51'51.36''	23.81	0.13	24.35	0.10
0 ^h 42 ^m 41.597 ^s	40°51'55.33''	24.13	0.21	24.17:	0.18
0 ^h 42 ^m 41.604 ^s	40°51'58.06''	24.40:	0.17	24.89	0.12
0 ^h 42 ^m 41.620 ^s	40°51'51.46''	24.27	0.18	24.84	0.18
0 ^h 42 ^m 41.642 ^s	40°51'55.96''	24.25	0.22	24.69:	0.26
0 ^h 42 ^m 41.642 ^s	40°51'52.14''	23.66	0.14	23.76	0.10
0 ^h 42 ^m 41.655 ^s	40°51'45.82''	24.27	0.16	25.37	0.14
0 ^h 42 ^m 41.662 ^s	40°51'52.37''	21.11	0.03	22.08	0.03
0 ^h 42 ^m 41.662 ^s	40°51'58.63''	22.54	0.05	22.83	0.03
0 ^h 42 ^m 41.671 ^s	40°51'56.12''	24.27	0.21	24.74:	0.25
0 ^h 42 ^m 41.674 ^s	40°51'44.44''	23.74	0.12	24.11:	0.10
0 ^h 42 ^m 41.681 ^s	40°51'55.88''	24.31	0.25	24.65:	0.33
0 ^h 42 ^m 41.702 ^s	40°51'56.45''	23.96	0.15	24.42	0.17
0 ^h 42 ^m 41.705 ^s	40°51'55.80''	24.08:	0.23	23.97	0.19
0 ^h 42 ^m 41.710 ^s	40°51'49.01''	24.00	0.13	24.52	0.09
0 ^h 42 ^m 41.711 ^s	40°51'57.54''	24.42	0.18	25.00:	0.16
0 ^h 42 ^m 41.711 ^s	40°51'47.49''	23.48	0.09	23.91	0.06
0 ^h 42 ^m 41.716 ^s	40°51'56.62''	23.80	0.13	24.27	0.13
0 ^h 42 ^m 41.724 ^s	40°51'50.72''	23.27	0.09	23.86	0.07
0 ^h 42 ^m 41.736 ^s	40°51'48.42''	24.19	0.15	24.72	0.10
0 ^h 42 ^m 41.748 ^s	40°51'45.06''	24.17	0.14	24.52	0.08
0 ^h 42 ^m 41.769 ^s	40°51'49.29''	24.49	0.20	25.24:	0.16
0 ^h 42 ^m 41.776 ^s	40°51'46.47''	23.99	0.13	24.79	0.09
0 ^h 42 ^m 41.778 ^s	40°51'57.86''	22.46	0.05	22.72	0.03
0 ^h 42 ^m 41.781 ^s	40°51'57.25''	24.09	0.14	24.84	0.13
0 ^h 42 ^m 41.782 ^s	40°51'48.78''	24.00:	0.14	25.04	0.13
0 ^h 42 ^m 41.787 ^s	40°51'56.88''	23.65:	0.11	24.13	0.09
0 ^h 42 ^m 41.793 ^s	40°51'52.60''	24.02	0.21	24.18	0.20
0 ^h 42 ^m 41.802 ^s	40°51'48.07''	24.47	0.19	24.66	0.09
0 ^h 42 ^m 41.820 ^s	40°51'52.46''	24.42:	0.24	24.68	0.26
0 ^h 42 ^m 41.824 ^s	40°51'55.73''	24.34	0.20	24.89	0.25
0 ^h 42 ^m 41.834 ^s	40°51'54.90''	22.23	0.05	22.77	0.05
0 ^h 42 ^m 41.837 ^s	40°51'52.53''	21.88	0.04	22.41	0.04
0 ^h 42 ^m 41.846 ^s	40°51'52.58''	23.48	0.11	24.31	0.16
0 ^h 42 ^m 41.851 ^s	40°51'54.30''	24.40	0.26	24.67:	0.27
0 ^h 42 ^m 41.856 ^s	40°51'46.48''	24.35	0.17	24.64	0.08
0 ^h 42 ^m 41.857 ^s	40°51'52.53''	22.14	0.05	22.88	0.05
0 ^h 42 ^m 41.863 ^s	40°51'55.18''	22.62	0.06	22.72	0.04
0 ^h 42 ^m 41.870 ^s	40°51'50.86''	24.40	0.19	24.95	0.16
0 ^h 42 ^m 41.873 ^s	40°51'57.90''	24.09:	0.15	25.41	0.17

TABLE 3—*Continued*

RA (J2000)	Dec (J2000)	m_{F175W} (mag)	error (mag)	m_{F275W} (mag)	error (mag)
$0^h42^m41.878^s$	$40^\circ51'50.27''$	22.43	0.05	23.20	0.04
$0^h42^m41.880^s$	$40^\circ51'46.79''$	24.29	0.16	25.12	0.12
$0^h42^m41.896^s$	$40^\circ51'54.22''$	24.07:	0.16	25.26	0.29
$0^h42^m41.900^s$	$40^\circ51'54.20''$	24.11:	0.17	25.08	0.23
$0^h42^m41.901^s$	$40^\circ51'49.36''$	23.35	0.09	23.48	0.05
$0^h42^m41.905^s$	$40^\circ51'45.29''$	23.76	0.12	24.82	0.09
$0^h42^m41.927^s$	$40^\circ51'55.02''$	24.20:	0.17	24.94	0.16
$0^h42^m41.940^s$	$40^\circ51'51.85''$	24.35	0.18	25.28	0.20
$0^h42^m41.953^s$	$40^\circ51'45.93''$	24.06	0.14	25.19:	0.18
$0^h42^m41.954^s$	$40^\circ51'51.37''$	24.18	0.16	24.43	0.09
$0^h42^m41.980^s$	$40^\circ51'52.83''$	23.21	0.08	23.71	0.06
$0^h42^m41.992^s$	$40^\circ51'53.93''$	24.21	0.16	24.73	0.12
$0^h42^m41.994^s$	$40^\circ51'57.50''$	24.13:	0.15	24.72	0.10
$0^h42^m41.995^s$	$40^\circ51'57.38''$	24.21:	0.16	24.95	0.12
$0^h42^m42.002^s$	$40^\circ51'53.24''$	23.46	0.10	23.94	0.07
$0^h42^m42.007^s$	$40^\circ51'50.54''$	24.48	0.20	24.72	0.10
$0^h42^m42.010^s$	$40^\circ51'49.33''$	22.72	0.06	23.58	0.05
$0^h42^m42.019^s$	$40^\circ51'55.44''$	23.81	0.12	24.59	0.10
$0^h42^m42.044^s$	$40^\circ51'53.33''$	24.49:	0.19	24.56	0.09
$0^h42^m42.045^s$	$40^\circ51'51.02''$	23.74	0.11	25.01	0.13
$0^h42^m42.085^s$	$40^\circ51'53.38''$	22.43	0.05	22.80	0.03
$0^h42^m42.088^s$	$40^\circ51'51.80''$	24.09:	0.15	25.15	0.14
$0^h42^m42.099^s$	$40^\circ51'54.88''$	24.45:	0.19	24.72	0.10
$0^h42^m42.107^s$	$40^\circ51'54.58''$	23.65	0.11	24.10	0.06
$0^h42^m42.147^s$	$40^\circ51'54.57''$	24.39	0.21	25.23:	0.14
$0^h42^m42.169^s$	$40^\circ51'56.97''$	24.20	0.17	24.33	0.08

TABLE 4: Comparison of *WFPC2* and *FOC* Integrated Photometry

(1) Galaxy	(2) Filter	(3) EXPTIME (sec)	(4) Gross count rate (cts s ⁻¹) ^a	(5) Dark count rate (cts s ⁻¹) ^a	(6) Sky count rate (cts s ⁻¹) ^a	(7) Net count rate (cts s ⁻¹) ^a	(8) Predicted Count rate (cts s ⁻¹) ^b	(9) Net/Predicted
M 31	F175W	19773	55.5	22.0	3.0	30.5	27.4	1.11
M 31	F275W	8390	228	22.0	7.6	198	229	0.86
M 31	F300W	3000	61.0	0	0.8	60.2	57.0	1.06
M 31	F336W	460	99.3	0	0.3	99.0	103	0.96
M 31	F555W	2200	4811	0	8.7	4802	≡4802	≡1
M 32	F175W	16179	97.9	22.0	3.0	72.9	68.0	1.07
M 32	F275W	8990	684	22.0	7.6	654	861	0.76
M 32	F300W	3000	230	0	0.8	229	206	1.11
M 32	F336W	1200	339	0	0.3	339	364	0.93
M 32	F555W	104	21019	0	17.4	21002	≡21002	≡1

^aMeasured count rate through a 2.8'' diameter circular aperture.^bPredicted count rate based upon the *IUE* spectrum, including red leak and normalized to agree in the visual (F555W).

TABLE 5: Photometry Characteristics

mag	Completeness (%) ^a				Standard Deviation (mag) ^a				Spurious sources (%) ^a			
	M 31		M 32		M 31		M 32		M 31		M 32	
	F175W	F275W	F175W	F275W	F175W	F275W	F175W	F275W	F175W	F275W	F175W	F275W
21.0	100	100	100	100	0.034	0.027	0.036	0.027	0	0	0	0
22.0	100	99	100	100	0.051	0.030	0.060	0.041	0	0	0	0
23.0	100	100	98	100	0.155	0.047	0.094	0.062	0	0	0	0
24.0	86	100	86	100	0.252	0.124	0.193	0.125	0	0	7	7
25.0	31	93	32	95	0.274	0.224	0.426	0.216	60	1	87	6
26.0	7	46	11	58	1.056	0.519	0.682	0.446	200	26	188	35

^aBeyond 1.5'' of the galactic center.

TABLE 6: Comparison of *FOC* and *IUE* fluxes

	M 31		M 32	
	F175W	F275W	F175W	F275W
(1) Gross count rate (cts s ⁻¹) ^a	1034	2694	1070	3551
(2) Dark count rate (cts s ⁻¹) ^b	637	637	637	637
(3) Sky count rate (cts s ⁻¹) ^c	87	219	87	219
(4) Net count rate (cts s ⁻¹) ^d	310	1838	346	2695
(5) Stellar count rate (cts s ⁻¹) ^d	14	61	3.1	12
(6) Predicted count rate (cts s ⁻¹) ^e	243	2031	279	3532
(7) Predicted UV count rate (cts s ⁻¹) ^f	78	1591	50	2929
(8) (Net <i>FOC</i>)/(UV+optical)	1.28	0.90	1.24	0.76
(9) (Stellar <i>FOC</i>)/UV	0.18	0.04	0.06	0.004

^aMeasured count rate through an artificial 10 × 20'' oval aperture (A+2B in Figures 4 & 5).

^bAssumed dark count rate through an artificial 10 × 20'' oval aperture (A+2B in Figures 4 & 5), assuming nominal *FOC* dark current.

^cAssumed sky count rate through an artificial 10 × 20'' oval aperture (A+2B in Figures 4 & 5), assuming average sky template spectrum.

^dMeasured count rate for stars in the artificial 10 × 20'' oval aperture (A+2B in Figures 4 & 5) and brighter than the limiting magnitudes.

^ePredicted count rate through a 10 × 20'' oval aperture, including red leak.

^fPredicted UV count rate through a 10 × 20'' oval aperture ($\lambda < 2400 \text{ \AA}$ in F175W and $\lambda < 3400 \text{ \AA}$ in F275W).

This figure "fig1.jpg" is available in "jpg" format from:

<http://arxiv.org/ps/astro-ph/9803327v1>

This figure "fig2.jpg" is available in "jpg" format from:

<http://arxiv.org/ps/astro-ph/9803327v1>